ANZIAM J. 59(2017), 1–34
doi:10.1017/S1446181117000256

ON MODELLING THE TRANSITION TO TURBULENCE IN PIPE FLOW

LAWRENCE K. FORBES ✉[1] and MICHAEL A. BRIDESON[1]

(Received 4 September, 2016; accepted 16 January, 2017; first published online 11 July 2017)

Abstract

As a possible model for fluid turbulence, a Reiner–Rivlin-type equation is used to study Poiseuille–Couette flow of a viscous fluid in a rotating cylindrical pipe. The equations of motion are derived in cylindrical coordinates, and small-amplitude perturbations are considered in full generality, involving all three velocity components. A new matrix-based numerical technique is proposed for the linearized problem, from which the stability is determined using a generalized eigenvalue approach. New results are obtained in this cylindrical geometry, which confirm and generalize the predictions of previous recent studies. A possible mechanism for the transition to turbulent flow is discussed.

2010 *Mathematics subject classification*: 76F06.

Keywords and phrases: circular pipe, linearization, Poiseuille flow, Reiner–Rivlin equations, stability analysis, transition to turbulence.

1. Introduction

This paper is concerned with attempting to develop a mathematical model that gives a consistent explanation for the phenomenon of fluid turbulence. It is necessary that the model should be based purely on the physics of the situation, and avoid heuristics or confusion between innate material properties (such as viscosity) and predicted fluid motion (such as velocity distributions). This is, of course, an enormously ambitious aim, and one which has occupied the attention of the best fluid dynamicists of the past century or more. Nevertheless, an underlying physical mechanism for the transition from well-ordered (laminar) flow to disordered turbulent flow remains unclear. As a result, it is, perhaps, not even possible to give a precise definition of what is meant by turbulent flow, although anyone who has ever observed the high-speed churning white-water being ejected from an outflow pipe into a river, for example, has an immediate intuitive understanding of the term.

[1]School of Mathematics and Physics, University of Tasmania, Tasmania, Australia;
e-mail: larry.forbes@utas.edu.au and michael.brideson@utas.edu.au.

There are two broad reasons for attempting to model turbulent flow, as is described very engagingly in the notes by George[1] [12]. The first reason is provided by the more immediate practical desire to simulate high-energy flows around aircraft wings or along coastlines, for example, and to account for the additional drag force, vorticity or energy loss seen in such flows, when these quantities are not well predicted by laminar-flow models governed by the Navier–Stokes equations. Since turbulent behaviour is observed to consist of a combination of a mean-field velocity $\overline{\mathbf{q}}$ that changes slowly with time, and an apparently random component $\mathbf{q}'$ that fluctuates rapidly in time and space, the Navier–Stokes equations are traditionally averaged, in an attempt to derive a new equation for the mean-field component $\overline{\mathbf{q}}$. This is, in fact, an approach that was originated by Reynolds [24]. However, because the Navier–Stokes equations involve a nonlinear convective term, the equation that is derived for the mean-field component $\overline{\mathbf{q}}$ is not "closed", in the sense that it also involves a term that consists of an averaged quadratic product $\overline{q_i' q_j'}$ of the rapidly changing component. Traditionally, this term is *modelled* using some hypothesis that expresses it purely in terms of the mean-field quantities. Details of such approaches are given by Davidson [6]. Early Reynolds-averaged turbulence models expressed the extra term simply as a standard diffusion term involving the mean-field velocity components, but multiplied by an "eddy viscosity" coefficient with a constant value μ_T much greater than the regular molecular viscosity μ. This is often not particularly successful in simulating experimental observations, and so later approaches regarded μ_T as a function of certain mean-field flow variables k and ε. In these "K-epsilon" models, each of these variables is supposed to be governed by its own convection–diffusion equation. Descriptions of such an approach are provided by Speziale [30] and Kitsios et al. [15]. In other models, moment-closure techniques are applied to derive an equation directly for the extra quadratic term $\overline{q_i' q_j'}$, and make use of statistical methods. These are described in review articles by McComb [17] and Cambon and Scott [4]. This class of modelling techniques for turbulence is not discussed further in this paper.

The second interest in turbulent flow is focussed more on modelling the physical causes of turbulence, and explaining the reasons for the transition from orderly laminar flow to turbulent flow, particularly as some critical speed (Reynolds number) is reached. This is the focus of the present paper. Traditionally, a simple solution to the Navier–Stokes equation is found, with steady velocity vector $\mathbf{q_0}$ and pressure p_0. Then a time-dependent perturbation is made to this solution, in which there is some small disturbance amplitude characterized by the parameter ϵ. Thus the velocity is expressed in the form $\mathbf{q} = \mathbf{q_0} + \epsilon\mathbf{q_1} + O(\epsilon^2)$, and the pressure becomes $p = p_0 + \epsilon p_1 + O(\epsilon^2)$. Linearized equations of motion for the perturbation quantities $\mathbf{q_1}$ and p_1 are generated by retaining only terms to first order in ϵ. These equations admit a time dependence in the form $\exp(-i\omega t)$, and so the sign of the imaginary part of the constant ω determines the stability of the zeroth-order solutions $\mathbf{q_0}$ and p_0. For flow in a circular cylindrical pipe, this process is described in detail by Drazin and

[1] The preface to this electronic book is particularly charming.

https://doi.org/10.1017/S1446181117000256 Published online by Cambridge University Press

Reid [7, Section 31.2]. They indicate that axi-symmetric flow in a circular cylindrical pipe is believed to be stable for all Reynolds numbers (flow speeds), and they present a typical eigenvalue distribution in the complex plane of the constant ω [7, p. 220].

In experimental observations of turbulent flow in a pipe, however, it is found that there appears to be a critical value of the Reynolds number beyond which a flow becomes unstable. While the exact value of this critical Reynolds number is in dispute, this fact has nevertheless led to a degree of dissatisfaction with linearized theory as described above, and the characterization of stability just in terms of the constant ω as the eigenvalue of a *linearized* system of equations for $\mathbf{q_1}$ and p_1. Trefethen et al. [33] have argued that even if the eigenvalue distribution suggests that the overall solution should be stable, the prediction is only really valid for arbitrarily large times t; initial conditions could cause solution modes to grow rapidly at early times and act as a trigger for nonlinear instability, even if they are ultimately stable as $t \to \infty$. Another somewhat obvious criticism of linearized theory is that perturbations to the background flow are assumed to be infinitesimally small, so that the eigenvalue-based predictions concerning stability are only strictly valid as $\epsilon \to 0$. But in a laboratory experiment, all perturbations must be finite in amplitude, so that even if the zeroth-order solution is linearly stable, it may fail to be nonlinearly stable to a small but finite-amplitude disturbance. Of course, such a criticism is always applicable to any linearization of a nonlinear process, and might therefore be of less immediate concern. Nevertheless, Cherubini et al. [5] have argued that there are purely *nonlinear* routes to instability in Navier–Stokes flows. It is known too that nonlinear finite-amplitude modes may also de-stabilize channel flows of visco-elastic fluids (Morozov and van Saarloos, [18]). Eckhardt [8, 9] has also indicated that the generation of turbulence might proceed primarily through nonlinear mechanisms, and Sano and Tamai [28] identify a "universal" route to turbulence that is characterized by the appearance of intermittent turbulent "spots" in the flow. In fact, Waleffe [36] had already shown numerically that the Navier–Stokes equations were capable of supporting coherent spatio-temporal structures in channel flow, which he identified as hallmarks of turbulence.

These criticisms of traditional stability theory are doubtless valid, and must affect the transition to unstable flow behaviour in Navier–Stokes flows. In a recent paper, Forbes [10] has also examined the consequences of replacing the Navier–Stokes equation with a slightly more general model of viscous fluid flow. After all, Navier–Stokes theory is predicated on the assumption that viscous strain rates are small enough that the constitutive law between the stress tensor $\mathbf{T}$ and strain-rate tensor $\mathbf{D}$ can be assumed to be purely *linear*, of the form $\mathbf{T} = -p\mathbf{I} + 2\mu\mathbf{D}$, in which $\mathbf{I}$ is the identity matrix, p is the fluid pressure and μ is its dynamic viscosity. This assumption is equivalent to Hooke's law in solid mechanics, and must be questionable for turbulent flows, which are characterized precisely by the development of large strain rates due to a high degree of local vorticity. Forbes [10] argued that the large strain rates encountered at small scales would mean that nonlinear terms in the constitutive relation between stress and strain rate could no longer be ignored in turbulent flows.

https://doi.org/10.1017/S1446181117000256 Published online by Cambridge University Press

This turns out to be consistent with the recent experimental results by Pelton et al. [21], who demonstrated that high-frequency vibrations at small length scales (perhaps comparable to Kolmogorov length scales) elicited a non-Newtonian response, even in "simple" fluids. Forbes [10] considered a more general constitutive law of the form $\mathbf{T} = -p\mathbf{I} + f(\mathbf{D})$, in which $f(x)$ is an analytic function of its argument. Since the strain-rate tensor $\mathbf{D}$ is a (3×3) matrix, Forbes argued that the function $f(x)$ only needed to contain a quadratically nonlinear term, so that $f(\mathbf{D}) = 2\mu\mathbf{D} + 2\tau\mathbf{D}^2$ without loss of generality. This results in the fluid being considered as a more general Stokes fluid (see Aris [2, Section 6.2]). The simplest description possible assumes that the two viscosities μ and τ may be assumed to be constants; then the Navier–Stokes description of the fluid behaviour is replaced by a Reiner–Rivlin equation, pioneered by Reiner [23] and Rivlin [25]. In fact, Rivlin [26] himself may have seen this equation as a means of describing turbulence. However, as indicated forcefully by Aris [2, p. 119], Reiner–Rivlin equations are extremely complicated, to the extent that serious analysis would appear impossible without sophisticated computer software.

Forbes [10] undertook a (semi-numerical) stability analysis of planar Poiseuille flow between two parallel plates, driven by a pressure gradient, and proposed a new possible explanation for the transition from laminar to turbulent flow. His stability analysis showed that for Reiner–Rivlin fluids the development of flow instability could occur in a very different manner to the usual situation for Navier–Stokes flow, in which instability arises when just a single eigenvalue ω develops an imaginary part that becomes positive, as in the celebrated calculations of Orszag [19]. The Reiner–Rivlin system reduces to the Navier–Stokes equations when the nonlinear viscosity coefficient τ is zero, and so of course the results then are identical. However, as τ increases, it is found that there is a critical value at which an entire line of eigenvalues in the complex ω-plane develop positive imaginary parts, so that the instability is now caused by very many eigenmodes, rather than just a single one. Furthermore, the real parts of these eigenvalues are not rational multiples of one another, with the result that, in this linearized theory, the solution would consist of an unstable quasi-periodic orbit of very high dimension. Nonlinear effects are then most likely to result in a cascade to a very high-dimensional chaotic state through a Ruelle–Takens–Newhouse bifurcation (see Thompson and Stewart [32, p. 196]). Forbes [10] conjectured this to be the origin of true fluid turbulence. Forbes also showed this to be a fundamentally three-dimensional effect, since he proved a theorem that the Reiner–Rivlin equation reduces exactly to Navier–Stokes behaviour for two-dimensional (planar) flows, for which this type of transition to instability cannot occur. In a later paper, Forbes [11] considered Reiner–Rivlin–Couette flow, in which a layer of fluid between parallel plates is caused to move by the movement of the plates. Qualitatively similar behaviour was encountered there also, and in this particularly simple geometry, Forbes [11] was able to carry out an asymptotic analysis for fluids dominated by the nonlinear viscous behaviour, and confirm analytically some features of the numerical solutions.

The destabilizing influence of nonlinear viscous effects is already known for some non-Newtonian visco-elastic fluids. What appears to be fully developed turbulence in

https://doi.org/10.1017/S1446181117000256 Published online by Cambridge University Press

certain polymer fluids, but at zero Reynolds number, has been observed experimentally by Larson [16]. Strong nonlinear instabilities may arise in visco-elastic fluids, and are discussed by Pan et al. [20] and Samanta et al. [27]. They may give rise to "elasto-inertial turbulence", caused by the interaction of the linear and nonlinear viscous effects in the Reiner–Rivlin equation. By considering that turbulence might be a weakly non-Newtonian effect, Forbes [10] suggested the possibility that some of these more exotic instances of visco-elastic turbulence might be part of the same mathematical solution branch as the more familiar fluid turbulence in high-speed fluids. If so, the only major difference between them would lie in the details of the material nonlinearity of the fluid in question, such as that measured by the nonlinear viscosity coefficient τ discussed above and in Section 2.

The present paper continues the initial investigation of Forbes [10], and considers Poiseuille flow of a Reiner–Rivlin fluid in a circular pipe, under a pressure gradient. In addition, the pipe itself may rotate about its own axis. This circular cylindrical geometry poses additional difficulties not encountered by Forbes [10], and the Reiner–Rivlin equations in this more complicated case are derived in Section 2. These equations are linearized about the basic Poiseuille–Couette flow in Section 3, to give a complicated set of linear differential equations analogous to the famous Orr–Sommerfeld equation discussed by Drazin and Reid [7]. The complexity of these equations, coupled with the additional difficulty associated with coordinate singularities on the axis $r = 0$ of the pipe, make the classical linear stability analysis of this system almost overwhelmingly complicated. After considerable experimentation, we have developed a matrix-based approach to this problem, combined with a particular spectral expansion in Bessel functions. This new numerical scheme is described in Section 4. Results are presented in Section 5, and a discussion in Section 6 concludes the paper.

2. The governing equations in cylindrical coordinates

2.1. Basic equations Consider an incompressible viscous Stokesian fluid of fixed density ρ. In cylindrical polar coordinates, its velocity vector is denoted $\mathbf{q} = u\mathbf{e_r} + v\mathbf{e}_\theta + w\mathbf{e_z}$. The usual relations apply between these cylindrical coordinates (r, θ, z) and the Cartesian system (x, y, z), so that

$$x = r\cos\theta, \quad y = r\sin\theta, \quad z = z.$$

The unit vectors $\{\mathbf{e_r}, \mathbf{e}_\theta, \mathbf{e_z}\}$ are written at each point in terms of the corresponding basis vectors $\{\mathbf{i}, \mathbf{j}, \mathbf{k}\}$ in Cartesian coordinates as

$$\begin{aligned}\mathbf{e_r} &= \cos\theta\mathbf{i} + \sin\theta\mathbf{j},\\ \mathbf{e}_\theta &= -\sin\theta\mathbf{i} + \cos\theta\mathbf{j},\\ \mathbf{e_z} &= \mathbf{k},\end{aligned}$$

and an important relation between the first two vectors in the cylindrical system is provided by the result

$$\frac{\partial \mathbf{e_r}}{\partial\theta} = \mathbf{e}_\theta \quad \text{and} \quad \frac{\partial \mathbf{e}_\theta}{\partial\theta} = -\mathbf{e_r}. \tag{2.1}$$

https://doi.org/10.1017/S1446181117000256 Published online by Cambridge University Press

Since the fluid is incompressible, its velocity vector $\mathbf{q}$ satisfies the continuity equation div$\mathbf{q} = 0$, which expressed in full gives

$$\frac{1}{r}\frac{\partial(ru)}{\partial r} + \frac{1}{r}\frac{\partial v}{\partial \theta} + \frac{\partial w}{\partial z} = 0. \tag{2.2}$$

Forbes [10, 11] has recently suggested that the transition from laminar to turbulent flow may not be a consequence of the Navier–Stokes equations alone, but rather may depend on the additional vorticity available from a more complex fluid model that allows some degree of non-Newtonian behaviour. Arguably, the simplest such system is a Reiner–Rivlin equation of the form

$$\frac{\partial \mathbf{q}}{\partial t} + (\mathbf{q}\cdot\nabla)\mathbf{q} + \frac{1}{\rho}\nabla p = \mathbf{f} + \frac{\mu}{\rho}\nabla^2\mathbf{q} + \frac{2\tau}{\rho}\mathrm{div}(\mathbf{D}^2). \tag{2.3}$$

Here, the fluid density is ρ and its usual dynamic viscosity is μ, as for the Navier–Stokes equation (see Batchelor [3, p. 147]), but now there is a second viscosity coefficient τ which is the coefficient of the non-Newtonian stress term. A derivation of this equation is given in the book by Aris [2] and the article by Forbes [10]. The pressure is p and the vector $\mathbf{f}$ represents the body force per mass acting on each fluid particle, whereas the (3×3) matrix

$$\mathbf{D} = \tfrac{1}{2}[(\nabla\mathbf{q}) + (\nabla\mathbf{q})^T] \tag{2.4}$$

is the strain-rate tensor. It turns out that equation (2.3) is a reasonably general description of the conservation of linear momentum for a non-Newtonian fluid without memory effects, for which the stress tensor $\mathbf{T}$ can be written as an analytic function of the rate-of-strain tensor $\mathbf{D}$ in equation (2.4). This is because any such nonlinear relation of the form $\mathbf{T} = f(\mathbf{D})$, in which the function f can be represented by a power series, can equivalently be written as a linear combination of the identity matrix and the first two powers $\mathbf{D}$ and $\mathbf{D}^2$ only, by virtue of the Cayley–Hamilton theorem (see Harman et al. [13, p. 183]).

2.2. Expression in cylindrical coordinates Even in Cartesian coordinates, the Reiner–Rivlin type equation (2.3) is not easy to write out in full (indeed, the text by Aris [2, p. 119] refers to the "appalling" complexity of the system). The task is even more difficult in cylindrical polar coordinates, because the derivatives of the basis vectors in equation (2.1) must also be taken into account, and care is required. Thus the dyadic tensor $\nabla\mathbf{q}$ in equation (2.4) becomes

$$\nabla\mathbf{q} = \frac{\partial \mathbf{q}}{\partial r}\mathbf{e_r} + \frac{1}{r}\frac{\partial \mathbf{q}}{\partial \theta}\mathbf{e}_\theta + \frac{\partial \mathbf{q}}{\partial z}\mathbf{e_z},$$

and the indicated derivatives involve both the velocity components and the basis vectors themselves. After some algebra, the (symmetric) strain-rate tensor (2.4) may be written as

$$\begin{aligned}\mathbf{D} = {} & D_{rr}\mathbf{e_r}\otimes\mathbf{e_r} + D_{\theta r}\mathbf{e}_\theta\otimes\mathbf{e_r} + D_{zr}\mathbf{e_z}\otimes\mathbf{e_r} \\ & + D_{\theta r}\mathbf{e_r}\otimes\mathbf{e}_\theta + D_{\theta\theta}\mathbf{e}_\theta\otimes\mathbf{e}_\theta + D_{z\theta}\mathbf{e_z}\otimes\mathbf{e}_\theta \\ & + D_{zr}\mathbf{e_r}\otimes\mathbf{e_z} + D_{z\theta}\mathbf{e}_\theta\otimes\mathbf{e_z} + D_{zz}\mathbf{e_z}\otimes\mathbf{e_z}.\end{aligned} \tag{2.5}$$

https://doi.org/10.1017/S1446181117000256 Published online by Cambridge University Press

The six independent components of this tensor are

$$\begin{aligned} D_{rr} &= \frac{\partial u}{\partial r}, & D_{\theta r} &= \frac{1}{2}\Big(\frac{\partial v}{\partial r} - \frac{v}{r} + \frac{1}{r}\frac{\partial u}{\partial \theta}\Big), \\ D_{zr} &= \frac{1}{2}\Big(\frac{\partial w}{\partial r} + \frac{\partial u}{\partial z}\Big), & D_{\theta\theta} &= \frac{1}{r}\Big(\frac{\partial v}{\partial \theta} + u\Big), \\ D_{z\theta} &= \frac{1}{2}\Big(\frac{\partial v}{\partial z} + \frac{1}{r}\frac{\partial w}{\partial \theta}\Big), & D_{zz} &= \frac{\partial w}{\partial z}, \end{aligned} \tag{2.6}$$

and outer products between two vectors are denoted using the symbol $\otimes$ in equation (2.5), following the notation of Kelly [14]. This outer product is itself a rank-one matrix, and is equivalent to the operation $\mathbf{a} \otimes \mathbf{b} = \mathbf{a}\mathbf{b}^T$ in matrix algebra.

It is convenient to denote the symmetric quadratic matrix product in (2.3) as $\mathbf{Q} = \mathbf{D}^2$ and its six independent components are

$$\begin{aligned} Q_{rr} &= D_{rr}^2 + D_{\theta r}^2 + D_{zr}^2, \\ Q_{\theta r} &= D_{\theta r}D_{rr} + D_{\theta\theta}D_{\theta r} + D_{z\theta}D_{zr}, \\ Q_{zr} &= D_{zr}D_{rr} + D_{z\theta}D_{\theta r} + D_{zz}D_{zr}, \\ Q_{\theta\theta} &= D_{\theta r}^2 + D_{\theta\theta}^2 + D_{z\theta}^2, \\ Q_{z\theta} &= D_{zr}D_{\theta r} + D_{z\theta}D_{\theta\theta} + D_{zz}D_{z\theta}, \\ Q_{zz} &= D_{zr}^2 + D_{z\theta}^2 + D_{zz}^2. \end{aligned} \tag{2.7}$$

The divergence of this tensor $\mathbf{Q}$ is now needed for use in the Reiner–Rivlin equation (2.3), differentiating also the unit vectors in the outer products $\mathbf{e_r} \otimes \mathbf{e_r}$ and so on, using equation (2.1). After a considerable amount of algebra, the three components of the (vector) momentum equation (2.3) are obtained in their final forms

$$\begin{aligned} &\frac{\partial u}{\partial t} + u\frac{\partial u}{\partial r} + \frac{v}{r}\frac{\partial u}{\partial \theta} - \frac{v^2}{r} + w\frac{\partial u}{\partial z} + \frac{1}{\rho}\frac{\partial p}{\partial r} \\ &\quad = f_R + \frac{\mu}{\rho}\Big[\frac{\partial^2 u}{\partial r^2} + \frac{1}{r}\frac{\partial u}{\partial r} + \frac{1}{r^2}\frac{\partial^2 u}{\partial \theta^2} + \frac{\partial^2 u}{\partial z^2} - \frac{u}{r^2} - \frac{2}{r^2}\frac{\partial v}{\partial \theta}\Big] \\ &\qquad + \frac{2\tau}{\rho}\Big[\frac{\partial Q_{rr}}{\partial r} + \frac{Q_{rr}}{r} + \frac{1}{r}\frac{\partial Q_{\theta r}}{\partial \theta} - \frac{Q_{\theta\theta}}{r} + \frac{\partial Q_{zr}}{\partial z}\Big] \end{aligned} \tag{2.8}$$

for the r-component of momentum conservation,

$$\begin{aligned} &\frac{\partial v}{\partial t} + u\frac{\partial v}{\partial r} + \frac{v}{r}\frac{\partial v}{\partial \theta} + \frac{uv}{r} + w\frac{\partial v}{\partial z} + \frac{1}{\rho r}\frac{\partial p}{\partial \theta} \\ &\quad = f_\Theta + \frac{\mu}{\rho}\Big[\frac{\partial^2 v}{\partial r^2} + \frac{1}{r}\frac{\partial v}{\partial r} + \frac{1}{r^2}\frac{\partial^2 v}{\partial \theta^2} + \frac{\partial^2 v}{\partial z^2} - \frac{v}{r^2} + \frac{2}{r^2}\frac{\partial u}{\partial \theta}\Big] \\ &\qquad + \frac{2\tau}{\rho}\Big[\frac{\partial Q_{\theta r}}{\partial r} + 2\frac{Q_{\theta r}}{r} + \frac{1}{r}\frac{\partial Q_{\theta\theta}}{\partial \theta} + \frac{\partial Q_{z\theta}}{\partial z}\Big] \end{aligned} \tag{2.9}$$

https://doi.org/10.1017/S1446181117000256 Published online by Cambridge University Press

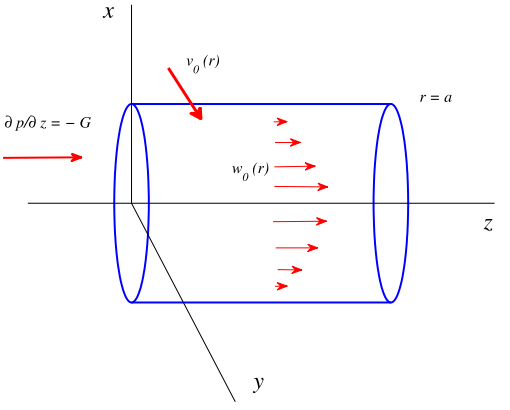

FIGURE 1. Schematic diagram of Poiseuille–Couette flow in a rotating cylinder.

for the azimuthal θ-component, and finally

$$\frac{\partial w}{\partial t} + u\frac{\partial w}{\partial r} + \frac{v}{r}\frac{\partial w}{\partial \theta} + w\frac{\partial w}{\partial z} + \frac{1}{\rho}\frac{\partial p}{\partial z} = f_Z + \frac{\mu}{\rho}\left[\frac{\partial^2 w}{\partial r^2} + \frac{1}{r}\frac{\partial w}{\partial r} + \frac{1}{r^2}\frac{\partial^2 w}{\partial \theta^2} + \frac{\partial^2 w}{\partial z^2}\right] + \frac{2\tau}{\rho}\left[\frac{\partial Q_{zr}}{\partial r} + \frac{Q_{zr}}{r} + \frac{1}{r}\frac{\partial Q_{z\theta}}{\partial \theta} + \frac{\partial Q_{zz}}{\partial z}\right] \quad (2.10)$$

for the z-component of momentum conservation. The convective and diffusive terms appearing in (2.8)–(2.10) are given by Batchelor [3, p. 602], and the body force per mass vector has components f_R , f_Θ and f_Z in the three coordinate directions. A Reiner–Rivlin-type flow is therefore a solution to the coupled system of equations (2.2), (2.8)–(2.10), subject to appropriate boundary conditions. In this paper, attention is focussed on flow in a circular pipe, and the aim is to study the possible transition to turbulent flow as a result of small perturbations to a steady-state solution.

2.3. Poiseuille–Couette flow Consider now the situation of classical Poiseuille flow, in which a pipe of radius a is positioned with the z-axis along its centre, and fluid is driven through it by an applied pressure gradient $\partial p/\partial z = -G$. Body forces are ignored. In addition, the pipe rotates with constant speed V_0 about the z-axis, in the azimuthal direction. A diagram of the flow configuration is sketched in Figure 1.

The flow is assumed to be steady, with no variation along the pipe and no dependence on the azimuthal angle θ. The continuity equation (2.2) then shows that the only solution with bounded radial velocity component u on the z-axis ($r = 0$) is simply $u = 0$. The axial momentum component (2.10) of the Reiner–Rivlin equation gives the classical result

$$w_0(r) = \frac{G}{4\mu}(a^2 - r^2) \quad (2.11)$$

for the fluid speed along the z-axis. This is Poiseuille flow (see Batchelor [3, p. 180]), and it satisfies the no-slip boundary condition

https://doi.org/10.1017/S1446181117000256 Published online by Cambridge University Press

$$w = 0 \quad \text{on } r = a \tag{2.12}$$

at the edge of the pipe.

The azimuthal component (2.9) of the momentum equation independently permits the solution

$$v_0(r) = \frac{V_0}{a} r \tag{2.13}$$

for the fluid speed in the θ-direction. The no-slip boundary condition in this case results in the requirement

$$v = V_0 \quad \text{on } r = a, \tag{2.14}$$

which is satisfied by the classical Couette flow (2.13).

Finally, the radial momentum equation (2.8) in this case shows that the pressure must take the form

$$p_0(r, z) = -Gz + \frac{1}{2}\rho\left[\left(\frac{V_0}{a}\right)^2 + \frac{3}{8}\frac{\tau}{\rho}\left(\frac{G}{\mu}\right)^2\right] r^2. \tag{2.15}$$

As for the plane Poiseuille flow problem discussed in Forbes [10], it is seen here that the two velocity components in (2.11) and (2.13) are identical to those predicted by the Navier–Stokes equation for this same situation. However, the pressure is not. There is an additional term in equation (2.15) proportional to r^2, and it is due to the additional coefficient τ of the non-Newtonian viscosity. This term persists in the absence of the rotation of the pipe ($V_0 = 0$), and so the uni-directional Poiseuille flow (2.11) might be able to be used *viscometrically*, in the sense outlined by Shaqfeh [29], as a means to measure the non-Newtonian coefficient τ through careful measurement of the wall pressure.

2.4. Planar flows In these cylindrical coordinates, planar two-dimensional flows are obtained when the axial velocity component is zero, $w = 0$, there is no axial dependence, $\partial/\partial z \equiv 0$, and no force component exists in that direction, $f_Z = 0$. It then follows from the continuity equation (2.2) that

$$D_{\theta\theta} = -\frac{\partial u}{\partial r} = -D_{rr}$$

in the components of the strain-rate tensor (2.6). As a result, the only nonzero components of the quadratic tensor $\mathbf{Q}$ in equation (2.7) are

$$Q_{\theta\theta} = Q_{rr} = D_{\theta r}^2 + D_{\theta\theta}^2.$$

In this case, the axial component (2.10) of the momentum equation is satisfied identically, and the radial and azimuthal components (2.8) and (2.9) reduce to

$$\begin{aligned} \frac{\partial u}{\partial t} + (\mathbf{q}\cdot\nabla_2)u - \frac{v^2}{r} + \frac{1}{\rho}\frac{\partial}{\partial r}(p - 2\tau Q_{rr}) &= f_R + \frac{\mu}{\rho}\left[\nabla_2^2 u - \frac{u}{r^2} - \frac{2}{r^2}\frac{\partial v}{\partial \theta}\right], \\ \frac{\partial v}{\partial t} + (\mathbf{q}\cdot\nabla_2)v + \frac{uv}{r} + \frac{1}{\rho r}\frac{\partial}{\partial \theta}(p - 2\tau Q_{rr}) &= f_\Theta + \frac{\mu}{\rho}\left[\nabla_2^2 v - \frac{v}{r^2} + \frac{2}{r^2}\frac{\partial u}{\partial \theta}\right], \end{aligned} \tag{2.16}$$

https://doi.org/10.1017/S1446181117000256 Published online by Cambridge University Press

in which the symbols ∇_2 and ∇_2^2 are the planar gradient and Laplacian operators, respectively.

Equation (2.16) is precisely the two-dimensional Navier–Stokes equation in polar coordinates, as given by Batchelor [3, p. 603], except that the pressure is replaced with the effective pressure

$$\Pi_{\text{eff}} = p - 2\tau Q_{rr}.$$

This confirms Forbes' [10] theorem that the Reiner–Rivlin equation (2.3) in two-dimensional flow reduces to the Navier–Stokes equation, but with an altered flow-dependent effective pressure. This, in turn, shows that Squire's theorem for the Navier–Stokes equation does not hold for Reiner–Rivlin type flows; Squire [31] proved that in the Navier–Stokes equations linearized about a base flow, a general three-dimensional perturbation could be regarded as a planar perturbation, only with an effective wavenumber made up from the two wavenumbers in orthogonal spatial directions. As a result, every three-dimensional disturbance is bounded above by an equivalent two-dimensional perturbation, so that planar flows define the general stability characteristics. This ceases to be true for non-Newtonian flows governed by an equation such as (2.3) since, while the two-dimensional form (2.16) is identical to a Navier–Stokes flow, the fully three-dimensional case is not, and instead has sources of instability and vorticity that are not equivalent to the corresponding Newtonian case (with $\tau = 0$).

2.5. Bi-streamfunction formulation The presence of the incompressible continuity equation (2.2) creates difficulties for the numerical solution of the system of governing equations in Section 2.1, and it is, therefore, desirable to satisfy continuity exactly, even in this fully three-dimensional flow.

For incompressible fluids, the continuity equation (2.2) is derived from $\text{div}\mathbf{q} = 0$, and this is solved exactly by any vector potential function $\mathbf{A}$ for which $\mathbf{q} = \text{curl}\mathbf{A}$. While many forms are possible for the vector potential, in the present case with cylindrical coordinates it is sufficient to define *two* streamfunctions $\Phi(r, \theta, z, t)$ and $\Psi(r, \theta, z, t)$ and take $\mathbf{A} = \Phi\mathbf{e}_\theta + \Psi\mathbf{e}_\mathbf{z}$. Then the three velocity components u, v and w in the radial, azimuthal and axial directions, respectively, may be expressed as

$$u = \frac{1}{r}\frac{\partial \Psi}{\partial \theta} - \frac{\partial \Phi}{\partial z}, \quad v = -\frac{\partial \Psi}{\partial r}, \quad w = \frac{1}{r}\frac{\partial (r\Phi)}{\partial r} \tag{2.17}$$

without any essential loss of generality. Thus, the three velocity components may be determined using only the two functions Φ and Ψ, and the relations (2.17) guarantee that (2.2) is satisfied as an identity. The three components of the Reiner–Rivlin equation (2.3) may thus be regarded as equations for the three unknown functions Φ, Ψ and the pressure p.

3. The linearized equations

In this paper, attention is focussed on the problem of Poiseuille–Couette flow in a circular rotating pipe, as illustrated in Figure 1. This requires solving the system of

https://doi.org/10.1017/S1446181117000256 Published online by Cambridge University Press

equations (2.8)–(2.10) in cylindrical polar coordinates for the two streamfunctions Φ and Ψ and the pressure p. A small perturbation to the solution in Section 2.3 is now considered, by expanding the velocity components and pressure in the form

$$\begin{aligned} u(r,z,\theta,t) &= \epsilon u_1(r,z,\theta,t) + O(\epsilon^2), \\ v(r,z,\theta,t) &= v_0(r) + \epsilon v_1(r,z,\theta,t) + O(\epsilon^2), \\ w(r,z,\theta,t) &= w_0(r) + \epsilon w_1(r,z,\theta,t) + O(\epsilon^2), \\ p(r,z,\theta,t) &= p_0(r,z) + \epsilon p_1(r,z,\theta,t) + O(\epsilon^2). \end{aligned} \tag{3.1}$$

Here, the base flow described by functions v_0, w_0 and p_0 is as given in equations (2.11), (2.13) and (2.15), respectively. As may be anticipated from Section 2.4 and the recent papers by Forbes [10, 11], fully three-dimensional flow will be needed in order to see the differences with Navier–Stokes theory, and this condition is met by the choice (3.1) for the linearized problem.

These forms (3.1) are substituted into the expressions (2.6) for the elements of the strain-rate tensor $\mathbf{D}$, the components (2.7) of the quadratic tensor $\mathbf{Q}$ and the governing continuity and momentum equations, and terms retained only to first order in the small parameter ϵ. This results in a system of four linear partial differential equations for the four perturbation functions u_1, v_1, w_1 and p_1 in equations (3.1), although the equations are lengthy, and so are not presented here. Following standard techniques such as those outlined by Drazin and Reid [7, p. 128], these functions are now further assumed to be of the Tollmien–Schlichting forms

$$\begin{aligned} u_1(r,z,\theta,t) &= \widetilde{U}_1(r)\exp[i(m\theta + kz - \omega t)], \\ v_1(r,z,\theta,t) &= \widetilde{V}_1(r)\exp[i(m\theta + kz - \omega t)], \\ w_1(r,z,\theta,t) &= \widetilde{W}_1(r)\exp[i(m\theta + kz - \omega t)], \\ p_1(r,z,\theta,t) &= \widetilde{P}_1(r)\exp[i(m\theta + kz - \omega t)]. \end{aligned} \tag{3.2}$$

The streamwise wavenumber k is related to the inverse of the wavelength of a perturbation down the pipe, in the axial z-direction. The quantity m essentially gives the mode number of disturbances in the azimuthal θ-coordinate, in the direction of rotation of the pipe. Since a unique value of the solution functions (3.2) is needed at each point, they must be 2π-periodic in θ, and therefore m must be an integer. The final constant ω in these expressions is, in general, a complex number of the form $\omega = \omega_R + i\omega_I$, and its value must be calculated from the governing equations and their boundary conditions, as an eigenvalue of the problem. Equations (3.2) show that disturbances grow with time like $\exp(\omega_I t)$, and thus the imaginary part ω_I of the eigenvalue ω determines stability. The perturbations (3.2) will decay, if $\omega_I < 0$ so that the Poiseuille–Couette flow in Section 2.3 will be stable; however, if $\omega_I > 0$ then the perturbations (3.2) in linearized theory will grow exponentially and the underlying flow will therefore be unstable.

The continuity equation (2.2) gives rise to the differential equation

$$\widetilde{U}_1' + \frac{1}{r}\widetilde{U}_1 + \frac{im}{r}\widetilde{V}_1 + ik\widetilde{W}_1 = 0 \tag{3.3}$$

https://doi.org/10.1017/S1446181117000256 Published online by Cambridge University Press

with the dash denoting differentiation with respect to r. It follows from (2.17) that this linearized continuity condition may be satisfied identically using two linearized streamfunctions $\widetilde{\Phi}_1(r)$ and $\widetilde{\Psi}_1(r)$ for which

$$\widetilde{U}_1 = \frac{im}{r}\widetilde{\Psi}_1 - ik\widetilde{\Phi}_1, \quad \widetilde{V}_1 = -\widetilde{\Psi}_1', \quad \widetilde{W}_1 = \widetilde{\Phi}_1' + \frac{1}{r}\widetilde{\Phi}_1. \tag{3.4}$$

Now the three components (2.8)–(2.10) of the Reiner–Rivlin momentum equation are likewise linearized, using the expansions (3.1) and the representations (3.2). The azimuthal component (2.9) when linearized may be expressed formally as

$$\frac{im}{r}\frac{1}{\rho}\widetilde{P}_1 = i\omega\widetilde{V}_1 + \mathbf{T}(r), \tag{3.5}$$

in which the function $\mathbf{T}(r)$ contains all the viscous and convective terms. Similarly, the linearized radial momentum equation derived from (2.8) takes the form

$$-i\omega\widetilde{U}_1 + \frac{1}{\rho}\widetilde{P}_1' = \mathbf{R}(r), \tag{3.6}$$

and the axial momentum component (2.10) of the Reiner–Rivlin equation linearizes to

$$-i\omega\widetilde{W}_1 + ik\frac{1}{\rho}\widetilde{P}_1 = \mathbf{Z}(r). \tag{3.7}$$

The three functions $\mathbf{T}$, $\mathbf{R}$ and $\mathbf{Z}$ are lengthy complicated expressions which, for completeness, are presented in the Appendix A. These three relations (3.5)–(3.7) are the equivalent of the Orr–Sommerfeld equation in more classical stability analyses of the Navier–Stokes equation (see Drazin and Reid [7, p. 156]).

4. Numerical solution of the linearized system

The structure of the linearized equations (3.5)–(3.7) permits a spectral series for the two streamfunction variables $\widetilde{\Phi}_1$ and $\widetilde{\Psi}_1$ and the reduced pressure variable $\widetilde{P}_1$. We have experimented with several representations for these functions, and have chosen a form which reduces numerical ill-conditioning, and which is consistent with the symmetries in the linearized system (3.5)–(3.7). In addition, the spectral representation must be capable of coping with the coordinate singularity on the z-axis $r = 0$. Accordingly, the three functions are formally expressed as

$$\begin{aligned}
\widetilde{\Psi}_1(r) &= \sum_{n=1}^{\infty} B_n J_m(\beta_{mn} r), \\
\widetilde{\Phi}_1(r) &= \sum_{n=1}^{\infty} A_n J_{m+1}(\alpha_{mn} r), \\
\frac{1}{\rho}\widetilde{P}_1(r) &= r\sum_{n=1}^{\infty} P_n J_m'(\beta_{mn} r).
\end{aligned} \tag{4.1}$$

In these expressions, the symbol J_ν represents the Bessel function of the first kind (see Abramowitz and Stegun [1]) of order ν, and J_ν' is its derivative with respect to its

https://doi.org/10.1017/S1446181117000256 Published online by Cambridge University Press

argument. The integer m is the Fourier mode in the Tollmien–Schlichting form (3.2) assumed for the solution. The constants

$$\beta_{mn} = \frac{j_{m,n}}{a} \quad \text{and} \quad \alpha_{mn} = \frac{j_{m+1,n}}{a} \tag{4.2}$$

also appear in the solution forms (4.1), in which the notation $j_{\nu,n}$ refers to the nth positive zero of the Bessel function J_ν. These series (4.1) may now be substituted into the expressions (3.4) to give similar formulae for the three velocity components.

The no-slip conditions (2.12) and (2.14) at the rotating wall at radius $r = a$ require that $\widetilde{U}_1(a) = \widetilde{V}_1(a) = \widetilde{W}_1(a) = 0$. The first of these conditions is identically satisfied by the series (4.1), but the remaining two conditions are yet to be satisfied. In addition, for numerical implementation, the series must be truncated at some finite order N. To illustrate the method for imposing the nonslip condition $\widetilde{V}_1(a) = 0$, an extra term at order $N + 1$ is initially retained in the series expression for $\widetilde{V}_1(r)$, so that its numerical form becomes

$$\widetilde{V}_1(r) = -\sum_{n=1}^{N} B_n \beta_{mn} J'_m(\beta_{mn} r) - B_{N+1} \beta_{m,N+1} J'_m(\beta_{m,N+1} r).$$

This expression is set to zero at $r = a$, thus giving the equation

$$B_{N+1} = -\sum_{n=1}^{N} B_n \frac{\beta_{mn}}{\beta_{m,N+1}} \mathcal{M}_{mn}$$

for the extra coefficient. Similarly, an extra term at order $N + 1$ is retained in the series expression for $\widetilde{W}_1$, so that when the condition $\widetilde{W}_1(a) = 0$ is imposed at the edge $r = a$ of the pipe, it leads to the equation

$$A_{N+1} = -\sum_{n=1}^{N} A_n \frac{\alpha_{mn}}{\alpha_{m,N+1}} \mathcal{N}_{mn}$$

for the additional term. In these expressions, and in later work, it is convenient to define the constants

$$\mathcal{M}_{mn} = \frac{J'_m(\beta_{mn} a)}{J'_m(\beta_{m,N+1} a)} \quad \text{and} \quad \mathcal{N}_{mn} = \frac{J'_{m+1}(\alpha_{mn} a)}{J'_{m+1}(\alpha_{m,N+1} a)}, \tag{4.3}$$

in which the constants β_{mn} and α_{mn}, $n = 1, 2, \ldots, N + 1$, are as defined in equation (4.2). As a consequence, every series expression involving coefficients B_{mn} and A_{mn} is extended in this way, so as to include the contribution at order $N + 1$ for consistency in the numerical scheme. No such provisions are required for the pressure function $\widetilde{P}_1(r)$ in equation (4.1), so the series for this function is simply truncated after the term of Nth order involving the coefficient P_N.

https://doi.org/10.1017/S1446181117000256 Published online by Cambridge University Press

It follows from equation (3.4) that the three velocity components have spectral representations in the forms

$$\begin{aligned}
\widetilde{U}_1(r) &= \frac{im}{r}\sum_{n=1}^{N} B_n T_n^{1b} - ik\sum_{n=1}^{N} A_n T_n^{1a},\\
\widetilde{V}_1(r) &= -\sum_{n=1}^{N} B_n T_n^{2b},\\
\widetilde{W}_1(r) &= \sum_{n=1}^{N} A_n T_n^{2a} + \frac{1}{r}\sum_{n=1}^{N} A_n T_n^{1a},
\end{aligned} \tag{4.4}$$

in which it is convenient to define further intermediate functions

$$\begin{aligned}
T_n^{1b}(r) &= J_m(\beta_{mn} r) - \frac{\beta_{mn}}{\beta_{m,N+1}}\mathcal{M}_{mn} J_m(\beta_{m,N+1} r),\\
T_n^{1a}(r) &= J_{m+1}(\alpha_{mn} r), -\frac{\alpha_{mn}}{\alpha_{m,N+1}}\mathcal{N}_{mn} J_{m+1}(\alpha_{m,N+1} r),\\
T_n^{2b}(r) &= \beta_{mn}[J'_m(\beta_{mn} r) - \mathcal{M}_{mn} J'_m(\beta_{m,N+1} r)],\\
T_n^{2a}(r) &= \alpha_{mn}[J'_{m+1}(\alpha_{mn} r) - \mathcal{N}_{mn} J'_{m+1}(\alpha_{m,N+1} r)].
\end{aligned} \tag{4.5}$$

To begin, the θ-momentum equation (3.5) is spectrally decomposed, by multiplying it by $r^2 J_m(\beta_{m\ell} r)$ and integrating over the domain $0 < r < a$. This gives rise to the expressions

$$\begin{aligned}
im\sum_{n=1}^{N} C_{\ell n}^{PT} P_n = -i\omega\sum_{n=1}^{N}\beta_{mn}[C_{\ell n}^{PT} - \mathcal{M}_{mn} C_{\ell,N+1}^{PT}]\, B_n\\
+ \int_0^a r^2 \mathbf{T}(r) J_m(\beta_{m\ell} r)\, dr, \quad \ell = 1, 2, \ldots, N.
\end{aligned} \tag{4.6}$$

In this expression, the constants

$$C_{\ell n}^{PT} = \int_0^a r^2 J'_m(\beta_{mn} r) J_m(\beta_{m\ell} r)\, dr \tag{4.7}$$

have been defined for convenience. Now the integral term on the right-hand side of (4.6) is formally a linear combination of the unknown coefficients B_n and A_n in the expressions (4.4), and so can be expressed as

$$\int_0^a r^2 \mathbf{T}(r) J_m(\beta_{m\ell} r)\, dr = \sum_{n=1}^{N} C_{\ell n}^{BT} B_n + \sum_{n=1}^{N} C_{\ell n}^{AT} A_n. \tag{4.8}$$

In a more traditional stability analysis of this type, the azimuthal momentum equation (3.5) would be used to eliminate the pressure function $\widetilde{P}_1(r)$ from the remaining two momentum equations (3.6) and (3.7) by substitution and cross-differentiation.

https://doi.org/10.1017/S1446181117000256 Published online by Cambridge University Press

This was the approach used by Forbes [10, 11]. However, the sheer volume of algebra involved makes this a task that is almost impossible to complete without errors of some type[1]. We used this traditional approach here at first, but extensive checking was needed using a computer-algebra package, and even this could not prevent numerical errors due to the ill-conditioning that arises from the addition and subtraction of large quantities of nearly equal magnitude. However, the recognition (4.8) that the integral term is able to be expressed in this way presents the opportunity to obtain the coefficients $C^{BT}_{\ell n}$ and $C^{AT}_{\ell n}$ numerically, in a fashion that is easy to implement, accurate, and avoids the cost of the formidable algebra otherwise incurred. To obtain these coefficients numerically, all that is needed is an accurate method for evaluating the integral on the left-hand side of equation (4.8); that is carried out here using Gaussian quadrature with 2501 points and the routine written by von Winckel [35]. Then, all the coefficients are set to zero except B_j which is given the value 1. The velocity components and their derivatives are then calculated from (4.4) and the function $\mathbf{T}$ is evaluated and the integral computed. This immediately gives the coefficient $C^{BT}_{\ell j}$ for $j = 1, 2, \ldots, N+1$ and for each $\ell = 1, 2, \ldots, N$. A similar procedure then yields $C^{AT}_{\ell j}$.

This matrix-based approach transforms the system (4.6) into the matrix–vector equation

$$im\mathbf{C}^{PT}\mathbf{P} = -i\omega\mathbf{E}^{BT}\mathbf{B} + \mathbf{C}^{BT}\mathbf{B} + \mathbf{C}^{AT}\mathbf{A}, \tag{4.9}$$

in which the $(N \times N)$ matrix $\mathbf{C}^{PT}$ is made up of components $C^{PT}_{\ell n}$ for $\ell, n = 1, 2, \ldots, N$ and the matrix $\mathbf{E}^{BT}$ has components $\beta_{mn}[C^{PT}_{\ell n} - \mathcal{M}_{mn}C^{PT}_{\ell N+1}]$. The remaining two $(N \times N)$ matrices $\mathbf{C}^{BT}$ and $\mathbf{C}^{AT}$ have components $C^{BT}_{\ell j}$ and $C^{AT}_{\ell j}$, respectively, computed numerically from (4.8) as described above, and the $(N \times 1)$ vectors $\mathbf{P}$, $\mathbf{B}$ and $\mathbf{A}$ are made up, respectively, from the coefficients P_n, B_n and A_n, $n = 1, 2, \ldots, N$, in the representations (4.1).

The radial momentum equation (3.6) is subjected to a similar Fourier analysis. The equation is multiplied by basis functions $J_m(\beta_{m\ell}r)$ and integrated over $0 < r < a$. This gives rise to equations

$$\begin{aligned}\omega m \sum_{n=1}^{N}\left[S^{BR}_{\ell n} - \frac{\beta_{mn}}{\beta_{m,N+1}}\mathcal{M}_{mn}S^{BR}_{\ell,N+1}\right]B_n - \omega k \sum_{n=1}^{N}\Bigg[S^{AR}_{\ell n} \\ - \frac{\alpha_{mn}}{\alpha_{m,N+1}}\mathcal{N}_{mn}S^{AR}_{\ell,N+1}\Bigg]A_n - \sum_{n=1}^{N} C^{PR}_{\ell n}P_n \\ = \int_0^a \mathbf{R}(r)J_m(\beta_{m\ell}r)\,dr, \quad \ell = 1, 2, \ldots, N,\end{aligned} \tag{4.10}$$

[1]We recall here Aris' [2] *cri de coeur* concerning the "appalling" complexity of even the Cartesian form of these equations.

https://doi.org/10.1017/S1446181117000256 Published online by Cambridge University Press

in which it is convenient to define further intermediate constants

$$S^{BR}_{\ell n} = \int_0^a \frac{1}{r} J_m(\beta_{mn} r) J_m(\beta_{m\ell} r)\, dr,$$
$$S^{AR}_{\ell n} = \int_0^a J_{m+1}(\alpha_{mn} r) J_m(\beta_{m\ell} r)\, dr, \tag{4.11}$$
$$C^{PR}_{\ell n} = \int_0^a \left[(\beta_{mn} r) - \frac{m^2}{(\beta_{mn} r)}\right] J_m(\beta_{mn} r) J_m(\beta_{m\ell} r)\, dr.$$

Once again, it is possible to avoid the formidable volume of algebra involved in isolating the coefficients B_n and A_n involved in this equation (4.10) using a numerical matrix-based approach, in which it is recognized that

$$\int_0^a \mathbf{R}(r) J_m(\beta_{m\ell} r)\, dr = \sum_{n=1}^N C^{BR}_{\ell n} B_n + \sum_{n=1}^N C^{AR}_{\ell n} A_n, \tag{4.12}$$

in which the desired coefficients can be determined by setting all the constants B_n and A_n to 0, except one which is instead set to 1, and simply reading off its coefficient as the value of the integral on the left-hand side of (4.12). This integral is evaluated to very high accuracy using numerical quadrature. As a result, the vector–matrix equation

$$\omega m \mathbf{E}^{BR}\mathbf{B} - \omega k \mathbf{E}^{AR}\mathbf{A} - \mathbf{C}^{PR}\mathbf{P} = \mathbf{C}^{BR}\mathbf{B} + \mathbf{C}^{AR}\mathbf{A} \tag{4.13}$$

is determined from (4.10). In this expression, the $(N \times N)$ matrices $\mathbf{C}^{PR}$, $\mathbf{C}^{BR}$ and $\mathbf{C}^{AR}$ are made up from the coefficients $C^{PR}_{\ell n}$ in equation (4.11) and $C^{BR}_{\ell n}$ and $C^{AR}_{\ell n}$ in equation (4.12), respectively. The remaining two matrices $\mathbf{E}^{BR}$ and $\mathbf{E}^{AR}$ have components

$$\left[S^{BR}_{\ell n} - \frac{\beta_{mn}}{\beta_{m,N+1}} \mathcal{M}_{mn} S^{BR}_{\ell,N+1}\right] \quad \text{and} \quad \left[S^{AR}_{\ell n} - \frac{\alpha_{mn}}{\alpha_{m,N+1}} \mathcal{N}_{mn} S^{AR}_{\ell,N+1}\right]$$

respectively, making further use of coefficients defined in (4.11).

In a similar manner, the axial momentum equation (3.7) is Fourier- analysed, by multiplying it by $rJ_m(\beta_{m\ell} r)$ and integrating over $0 < r < a$. This gives the further system of equations

$$\omega \sum_{n=1}^N \left[S^{AZ}_{\ell n} - \frac{\alpha_{mn}}{\alpha_{m,N+1}} \mathcal{N}_{mn} S^{AZ}_{\ell,N+1}\right] A_n - k \sum_{n=1}^N C^{PT}_{\ell n} P_n$$
$$= i \int_0^a r \mathbf{Z}(r) J_m(\beta_{m\ell} r)\, dr, \quad \ell = 1, 2, \ldots, N. \tag{4.14}$$

In this expression, the coefficients $C^{PT}_{\ell n}$ are as defined previously in (4.7), and the additional constants

$$S^{AZ}_{\ell m} = \int_0^a [(\alpha_{mn} r) J'_{m+1}(\alpha_{mn} r) + J_{m+1}(\alpha_{mn} r)] J_m(\beta_{m\ell} r)\, dr \tag{4.15}$$

https://doi.org/10.1017/S1446181117000256 Published online by Cambridge University Press

have also been defined. In addition, the integral term in (4.14) can be decomposed numerically into an expression of the form

$$\int_0^a r\mathbf{Z}(r)J_m(\beta_{m\ell}r)\,dr = \sum_{n=1}^{N} C_{\ell n}^{BZ}B_n + \sum_{n=1}^{N} C_{\ell n}^{AZ}A_n, \tag{4.16}$$

in which the sets of coefficients $C_{\ell n}^{BZ}$ and $C_{\ell n}^{AZ}$ are obtained using numerical quadrature and the technique of making only one of the constants B_n, A_n at a time be nonzero, with a value of 1, as described previously. Consequently, equation (4.14) yields the matrix system

$$\omega\mathbf{E}^{AZ}\mathbf{A} - k\mathbf{C}^{PT}\mathbf{P} = i\mathbf{C}^{BZ}\mathbf{B} + i\mathbf{C}^{AZ}\mathbf{A}, \tag{4.17}$$

in which the $(N \times N)$ matrix $\mathbf{E}^{AZ}$ has components

$$\left[S_{\ell n}^{AZ} - \frac{\alpha_{mn}}{\alpha_{m,N+1}}\mathcal{N}_{mn}S_{\ell,N+1}^{AZ}\right].$$

The three vector equations (4.9), (4.13) and (4.17) constitute a generalized eigenvalue problem for an eigenvector consisting of components P_n, B_n and A_n and eigenvalue ω. However, it is not suitable to be used in this form, because the eigenvalue ω does not multiply the coefficients P_n in any of these equations, and as a result, the system contains infinite eigenvalues, and is too ill-conditioned to give meaningful results. This is a difficulty that is reasonably well understood in the rheological literature, and is discussed by Valério et al. [34]. To overcome this problem, the coefficients P_n must be solved for, using equation (4.9), and eliminated from the remaining two equations (4.13) and (4.17). As discussed previously, this would normally constitute a prohibitively large amount of algebra, but the numerical matrix formulation used here makes the task reasonably straightforward. This gives rise to the block matrix problem

$$\begin{bmatrix}\mathbf{W}^{BR} & \mathbf{W}^{AR}\\ \mathbf{W}^{BZ} & \mathbf{W}^{AZ}\end{bmatrix}\begin{bmatrix}\mathbf{B}\\ \mathbf{A}\end{bmatrix} = \omega\begin{bmatrix}\mathbf{X}^{BR} & -km\mathbf{E}^{AR}\\ k\mathbf{E}^{BT} & m\mathbf{E}^{AZ}\end{bmatrix}\begin{bmatrix}\mathbf{B}\\ \mathbf{A}\end{bmatrix}. \tag{4.18}$$

This is a generalized eigenvalue problem, which, for given azimuthal vibration number m and axial wavenumber k, is to be solved for the eigenvector $[\mathbf{B}\,\mathbf{A}]^T$ and the eigenvalue ω. The mode is stable, if every eigenvalue ω has negative imaginary part. In this expression (4.18), the additional $(N \times N)$ matrices needed are defined as

$$\begin{aligned}
\mathbf{W}^{BR} &= m\mathbf{C}^{BR} - i\mathbf{C}^{PR}[\mathbf{C}^{PT}]^{-1}\mathbf{C}^{BT},\\
\mathbf{W}^{AR} &= m\mathbf{C}^{AR} - i\mathbf{C}^{PR}[\mathbf{C}^{PT}]^{-1}\mathbf{C}^{AT},\\
\mathbf{W}^{BZ} &= im\mathbf{C}^{BZ} - ik\mathbf{C}^{BT},\\
\mathbf{W}^{AZ} &= im\mathbf{C}^{AZ} - ik\mathbf{C}^{AT},\\
\mathbf{X}^{BR} &= m^2\mathbf{E}^{BR} + \mathbf{C}^{PR}[\mathbf{C}^{PT}]^{-1}\mathbf{E}^{BT}.
\end{aligned}$$

This generalized eigenvalue problem (4.18) is solved using the eigenvalue routine `eig` in the numerical package *MATLAB*. The algorithm is run typically using 2501

https://doi.org/10.1017/S1446181117000256 Published online by Cambridge University Press

points distributed over the interval $0 < r/a < 1$ and the number of modes N between 101 and 401. The integrals in equations (4.7), (4.8), (4.11), (4.12), (4.15) and (4.16) are all carried out using Gauss–Legendre quadrature as implemented in the routine by von Winckel [35], over the 2501 numerical points that the routine generates over $0 < r/a < 1$.

5. Presentation of results

It is convenient in this presentation of results to nondimensionalize the equations in the above analysis. In view of the complexity of these systems, details will not be given here, except to indicate that all lengths are scaled with respect to the pipe radius a and speeds are made dimensionless using the quantity βa^2, in which $\beta = G/(4\mu)$ and G is the pressure gradient driving the flow in equation (2.11). The constant μ is the usual (Newtonian) dynamic viscosity. Consequently, there are five dimensionless constants that describe the solutions to this problem. The first three are related to the details of the fluid motion, and are

$$K = ak, \quad \Omega = \frac{\omega}{\beta a}, \quad \gamma = \frac{1}{\beta a}\left(\frac{V_0}{a}\right),$$

in which V_0 is the azimuthal velocity component of the rotating pipe. The constant K is the dimensionless wavenumber in the axial direction and γ is the rotation speed parameter of the pipe. The dimensionless frequency Ω is the eigenvalue, for which the imaginary part determines the stability of the mth rotation mode. There are a further two dimensionless constants

$$\frac{1}{R_e} = \frac{1}{\beta a^3}\left(\frac{\mu}{\rho}\right), \quad \frac{1}{F} = \frac{4}{a^2}\left(\frac{\tau}{\rho}\right)$$

which describe the properties of the material. The constant R_e is a Reynolds number based on the Newtonian viscosity μ, the characteristic speed at the centre of the pipe due to the imposed pressure gradient, and the radius of the pipe. The second parameter F is a dimensionless measure of the effect of the second coefficient τ of nonlinear viscosity, and was introduced by Forbes [10]. It would instead have been possible to use the Weissenberg or Deborah numbers (see Poole [22]), but the parameter F is preferred here, because it is independent of the Newtonian viscosity coefficient μ. The two material extremes in the Reiner–Rivlin model (2.3) are therefore $F = \infty$ representing a purely Newtonian flow described by the Navier–Stokes equation, and $R_e = \infty$ which corresponds to a fluid dominated by nonlinear viscosity.

Figure 2 shows the eigenvalues computed for the purely Newtonian flow $1/F = 0$, for the third azimuthal mode $m = 3$ at Reynolds number $R_e = 1000$. The low mode numbers $K = m = 3$ have been chosen in this instance to give behaviour that is very similar to that shown by Drazin and Reid [7, p. 220]. This is a classically stable flow, as is evident from the fact that all the computed eigenvalues lie in the half-space $\mathrm{Im}\{\Omega\} < 0$. As a check on the accuracy of the method, eigenvalues have been computed with $N = 101$ and $N = 201$ Fourier modes, and the agreement between the

https://doi.org/10.1017/S1446181117000256 Published online by Cambridge University Press

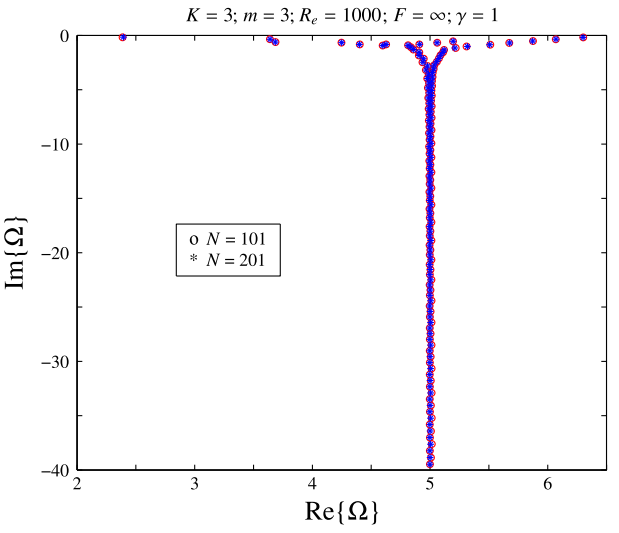

FIGURE 2. Eigenvalue distribution in the complex Ω-plane, for a purely Newtonian viscous flow ($F = \infty$) for Reynolds number $R_e = 1000$, wavenumber $K = 3$, rotation rate $\gamma = 1$, at the third azimuthal mode $m = 3$.

two sets of results over the region indicated is excellent. In the case $N = 201$ there are additional eigenvalues that lie on the approximate vertical line $\mathrm{Re}\{\Omega\} = 5$, but extending well below the region indicated in Figure 2. These additional eigenvalues may be spurious, but since they are deeply embedded in the stable region $\mathrm{Im}\{\Omega\} < 0$, they have no influence on the stability of the Reiner–Rivlin–Couette flow. In this picture, the rotation rate has been set to $\gamma = 1$, although many other values for this parameter have been tried. It is found that, at moderate values, γ has very little effect on the location of the eigenvalues and therefore no major influence on stability, although very large values of γ move the eigenvalues down the diagram somewhat, so making the solution more stable. This is possibly to be expected on physical grounds, since a flow dominated by rapid rotation about the central z-axis is more stable to small disturbances.

The other extreme is illustrated in Figure 3. Here, the usual viscosity terms, with coefficient μ in equations (3.5)–(3.7), are absent from the momentum equations, so that the only remaining viscous term is the one involving τ, describing material nonlinearity. For this infinite Reynolds number case, $R_e = \infty$, it is found that $N = 201$ Fourier modes are needed, to give sufficient accuracy for the eigenvalues Ω. As described by Forbes [11], it is mostly only the eigenvalues closer to the real axis that are reliable; while many occur with $|\mathrm{Im}\{\Omega\}|$ large, they are mostly numerically generated, since they vary with increasing number N of Fourier coefficients. This is visible in Figure 3, where the numerical algorithm of Section 4 has been run both for $N = 201$ and $N = 401$ Fourier modes. The two horizontal lines of eigenvalues, at about $\mathrm{Im}\{\Omega\} = \pm 1$, are highly converged and represent genuine eigenmodes for the linearized

https://doi.org/10.1017/S1446181117000256 Published online by Cambridge University Press

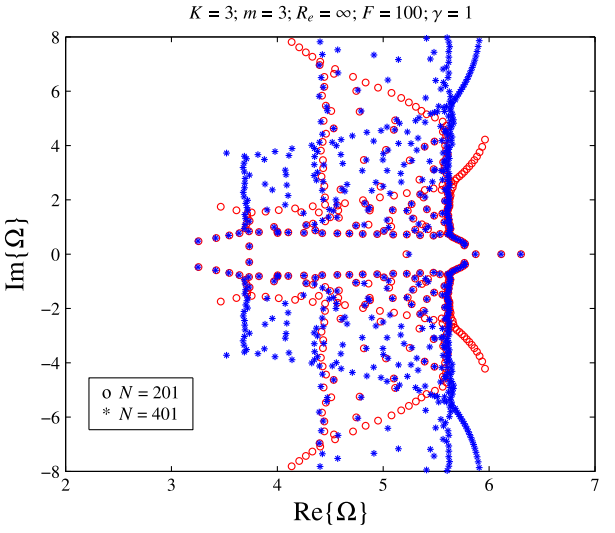

FIGURE 3. Eigenvalue distribution in the complex Ω-plane, for a purely elastic viscous flow ($R_e = \infty$) for nonlinear viscosity $F = 100$, wavenumber $K = 3$, rotation rate $\gamma = 1$, at the third azimuthal mode $m = 3$.

problem in Section 3. This is also true of a section of the two vertical lines at about $\mathrm{Re}\{\Omega\} = 5.6$, where again the eigenvalues are highly converged and may even occur as a continuum, although this is not certain.

The other main feature of note in Figure 3 is that the eigenvalues Ω appear to be symmetrically placed about the real axis. This is, in fact, correct, and it leads to an important result, which defines the role of the nonlinear viscous terms in the Reiner–Rivlin equation (2.3). This is summarized in the following theorem.

THEOREM 5.1. *Poiseuille–Couette flow is always unstable for sufficiently large Reynolds number.*

PROOF. This result follows at once from the fact that the eigenvalues ω of the linearized system of equations (3.3), (3.5)–(3.7) with $\mu = 0$ occur in *complex conjugate pairs*. To see this, first take the complex conjugate of each of these equations, and then observe that the original equations are recovered with new eigenvalue and new velocity components $(\omega^*, U^*, V^*, W^*)$ defined by the relations

$$\omega^* = \overline{\omega}, \quad U^* = -\overline{\widetilde{U}_1}, \quad V^* = \overline{\widetilde{V}_1}, \quad W^* = \overline{\widetilde{W}_1}, \quad P^* = \overline{\widetilde{P}_1}. \tag{5.1}$$

Here, the overline $\overline{\omega}$, and so on, denotes the complex conjugate. Because the momentum equations (3.5)–(3.7) with the additional functions (A.1)–(A.3), are extremely lengthy, the proof of this remark will only be illustrated here for the simpler case of the linearized continuity equation (3.3). The complex conjugate of the entire equation becomes

$$\overline{\widetilde{U}_1'} + \frac{1}{r}\overline{\widetilde{U}_1} - \frac{im}{r}\overline{\widetilde{V}_1} - ik\overline{\widetilde{W}_1} = 0.$$

https://doi.org/10.1017/S1446181117000256 Published online by Cambridge University Press

Now making the transformations of variables indicated in equations (5.1) reduces this to

$$U^{*\prime} + \frac{1}{r}U^* + \frac{im}{r}V^* + ikW^* = 0,$$

which is just the original continuity equation (3.3) in the new variables in equation (5.1). Similar results may be shown in a straightforward manner for the three momentum components (3.5)–(3.7), after substantial algebra. Thus, if ω is an eigenvalue, then so is its complex conjugate $\overline{\omega}$. Therefore, there are always eigenvalues with $\mathrm{Im}\{\Omega\} > 0$ for $R_e = \infty$, so that the solution is always unstable. □

It follows from Theorem 5.1 that the additional nonlinear viscosity τ has a destabilizing effect on the pipe flow. This is counteracted by the dynamic viscosity μ which damps small disturbances due to its diffusive effect, as expected. When μ is large (Reynolds number R_e is small), the damping effect dominates and the flow is stable. However, as μ decreases (R_e increases), the eigenvalues move up towards the unstable region $\mathrm{Im}\{\Omega\} > 0$, and for sufficiently small μ (large R_e) elastic material nonlinearity effects begin to dominate, and the distribution of eigenvalues becomes more similar to that in Figure 3. Importantly in this Reiner–Rivlin model of fluid motion, for sufficiently large Reynolds number, a very large number of eigenvalues moves into the unstable region, so that the flow behaviour produced by this linearized problem consists of an unstable quasi-periodic structure of very high dimension. This is the situation regarded by Forbes [10, 11] as being representative of the transition to true turbulence, since the re-introduction of even moderate nonlinearity would cause the high-dimensional quasi-periodic structure to collapse into a high-dimensional chaotic strange attractor, through the mechanism of Ruelle–Takens–Newhouse bifurcation (Thompson and Stewart, [32, p. 196]).

Following Forbes [11], we have created a stability diagram in Figure 4, for wave and mode numbers $K = m = 20$ and dimensionless rotation speed $\gamma = 0.1$. Similar results have been generated for other modes, and the higher values $K = m = 20$ have been chosen here somewhat arbitrarily for their more interesting eigenvalue patterns, illustrated later. Different rotation speeds γ have also been investigated, but moderate values, including zero, produce stability diagrams that are very similar to the one shown here.

There are three zones illustrated in Figure 4, corresponding to three markedly different mathematical structures. The first is the left-most region shaded darkly (green online). In this zone, all the eigenvalues Ω have negative imaginary parts, so that the overall solutions are stable for parameter values R_e and F in this region. The central lightly shaded (fawn online) region of parameter space is characterized by the fact that a small number of eigenvalues Ω have ventured into the region of instability $\mathrm{Im}\{\Omega\} > 0$ in the complex eigenvalue plane, so that the solution is now weakly unstable to a small number of Fourier modes in the representation (4.1). In the final unshaded region to the right of Figure 4, marked “turbulent”, a very large number of eigenvalues has crossed into the unstable region of the complex Ω-plane, so that the corresponding solution involves an unstable quasi-periodic orbit of very high dimension. This is the

https://doi.org/10.1017/S1446181117000256 Published online by Cambridge University Press

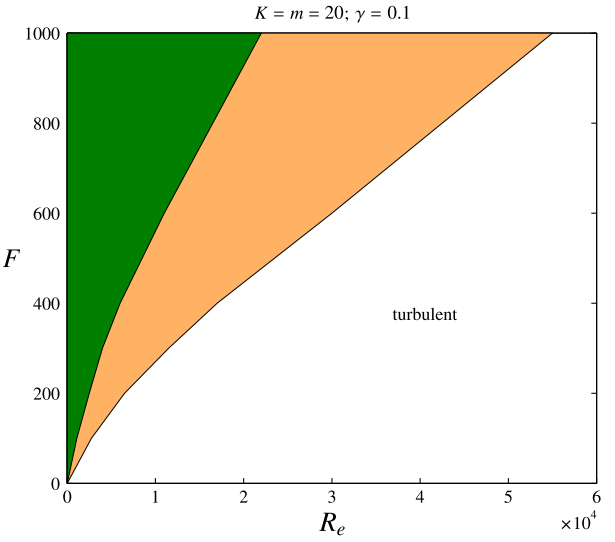

FIGURE 4. Stability region in the (R_e, F) parameter plane, for wavenumber $K = 20$, rotation rate $\gamma = 0.1$, at mode number $m = 20$. The solutions are stable in the (green online) region on the left, unstable to a small number of modes in the central (fawn online) region, and a high-dimensional quasi-periodic solution is produced in the region marked "turbulent" on the right.

zone identified by Forbes [10] as leading to genuine turbulence, since nonlinearity in the full system of equations would cause a chaotic attractor of very high dimension to form. The two boundaries between these three zones are indicated with thin dark lines in Figure 4, and were estimated by monitoring a large number of computer runs, and estimating the approximate points of transition. This is necessarily only a crude estimate by eye, and involves a certain degree of subjective value judgement as to what represents a true solution of the type on one side of the boundary or the other. Thus the sizes of the regions shown in Figure 4 are approximate only and therefore subject to criticism, but they do at least give a qualitative understanding of the three behaviour types possible in the linearized solution.

A further illustration of the numerical convergence of the eigenvalues is given in Figure 5, for a case in which the Reynolds number R_e and the nonlinear viscosity parameter F are both finite. With $N = 201$ Fourier modes, the solution is highly converged, at least for the significant eigenvalues at the top of the diagram, since there is excellent agreement with the results with $N = 401$ eigenmodes. For this larger number $N = 401$ of modes, there are additional eigenvalues that extend deeply into the stable region $\mathrm{Im}\{\Omega\} < 0$ below the portion shown in Figure 5, similar to the situation described for Figure 2. These, however, have no effect on stability and so are not of primary interest.

To illustrate further the information encoded in Figure 4, we consider the horizontal slice through Figure 4 at the value $F = 600$ of the dimensionless material nonlinearity coefficient, at four different values of the Reynolds number R_e. These four solutions

https://doi.org/10.1017/S1446181117000256 Published online by Cambridge University Press

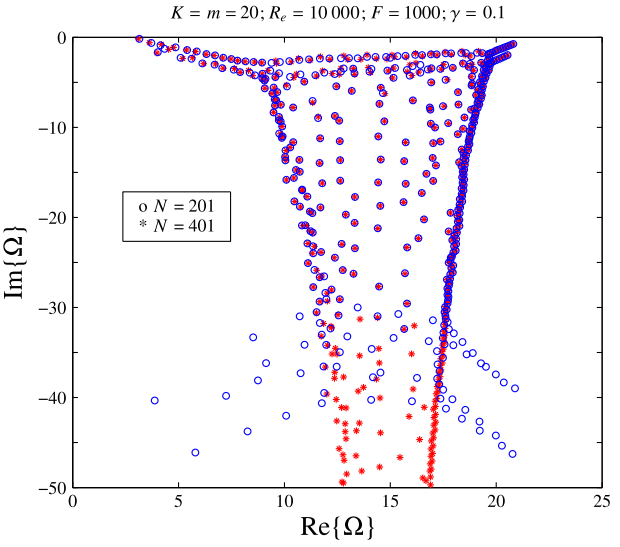

FIGURE 5. Eigenvalue distribution in the complex Ω-plane, for a Reiner–Rivlin viscous flow with Reynolds number $R_e = 10\,000$, nonlinear viscosity parameter $F = 1000$, wavenumber $K = 20$, rotation rate $\gamma = 0.1$, at azimuthal mode number $m = 20$.

are presented in Figure 6. The first of these, for $R_e = 5000$ in Figure 6(a), lies safely within the dark (green online) region on the left of Figure 4, and so is stable. This is immediately evident from Figure 6(a), since all the eigenvalues Ω lie in the stable zone $\mathrm{Im}\{\Omega\} < 0$ below the (red online) arrow at the left of the diagram, similar to the situation illustrated in Figure 5. Figure 6(b) shows the eigenvalue distribution for the situation in which the Reynolds number has increased to the value $R_e = 11\,000$. At about this value the solution first begins to become unstable, since a single eigenvalue crosses the stability boundary $\mathrm{Im}\{\Omega\} = 0$ indicated with the arrow. This solution is approximately on the boundary between the (green online) darkly shaded region and the (fawn online) lightly shaded regions in Figure 4. As Reynolds number continues to increase beyond this border value $R_e = 11\,000$ a few more eigenvalues cross into the unstable zone $\mathrm{Im}\{\Omega\} > 0$, so that the solution contains a small number of modes that grow reasonably slowly with time, and so are unstable.

The next solution illustrated in Figure 6(c) is for the smallest value of Reynolds number $R_e = 30\,000$, at which an entire line of eigenvalues has crossed into the unstable zone. It therefore represents a solution on about the second border in Figure 4, between the middle lightly shaded (fawn online) region and the right-most unshaded region labelled "turbulent". It must be admitted frankly that the precise location of this boundary is very debatable, since already there are many eigenvalues from that upper branch that are in the unstable zone $\mathrm{Im}\{\Omega\} > 0$, and so it is possible that this second border should perhaps be positioned at a lower Reynolds number. Somewhat arbitrarily, we have taken the border between these two unstable solution zones in

https://doi.org/10.1017/S1446181117000256 Published online by Cambridge University Press

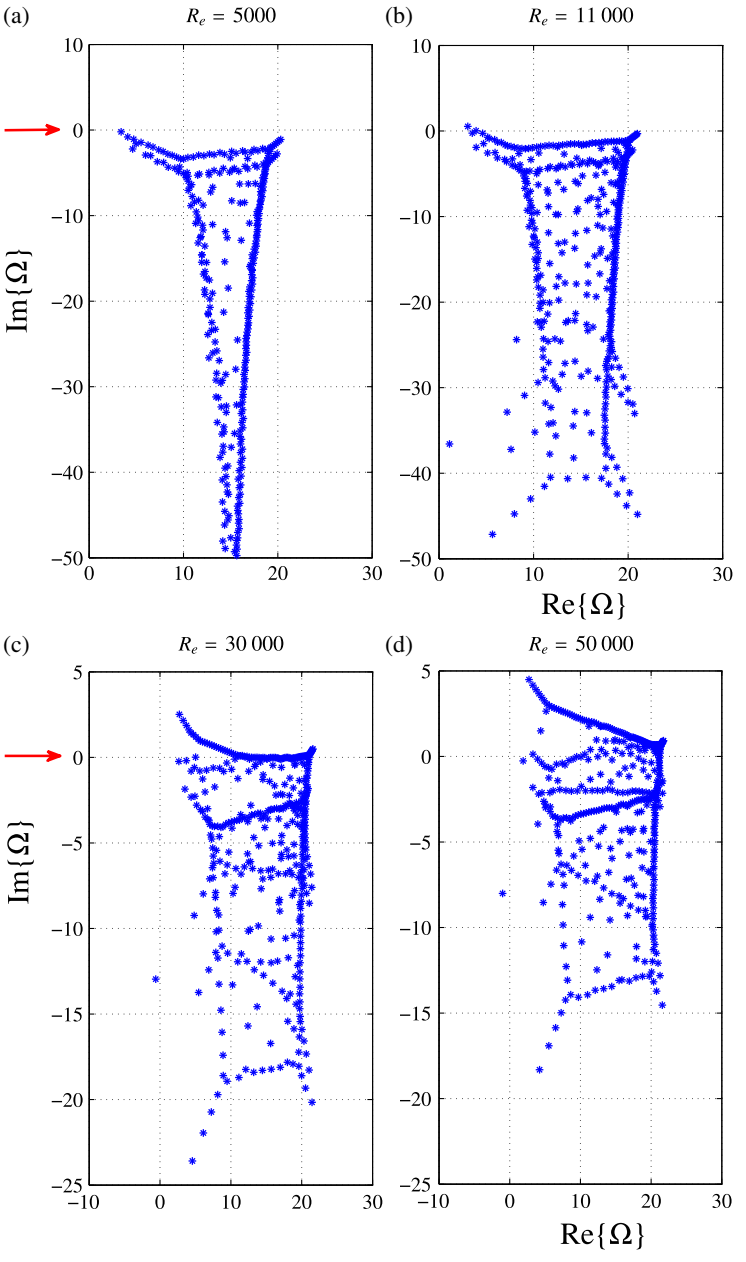

FIGURE 6. Eigenvalue distribution in the complex Ω-plane, for four different Reynolds numbers, with wavenumber $K = 20$, rotation rate $\gamma = 0.1$, mode number $m = 20$ and nonlinear viscosity parameter $F = 600$. Solutions are shown for Reynolds numbers (a) $R_e = 5000$, (b) $R_e = 11\,000$, (c) $R_e = 30\,000$ and (d) $R_e = 50\,000$. The (red online) arrow at the left of each set of diagrams shows the stability boundary $\mathrm{Im}\{\Omega\} = 0$.

https://doi.org/10.1017/S1446181117000256 Published online by Cambridge University Press

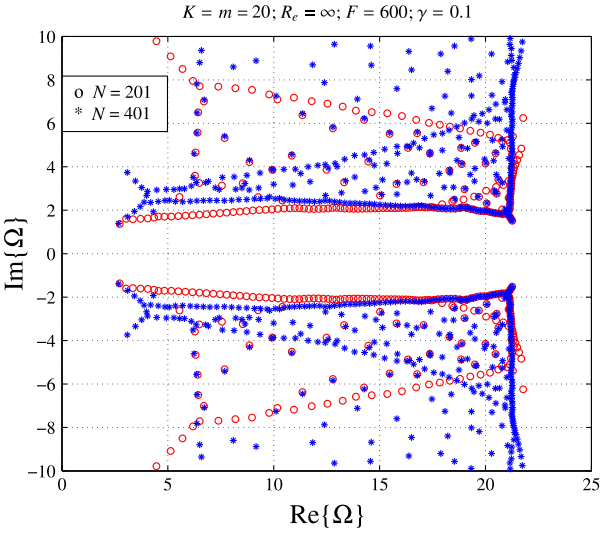

FIGURE 7. Eigenvalue distribution in the complex Ω-plane, for a purely elastic viscous flow ($R_e = \infty$) for nonlinear viscosity $F = 600$, wavenumber $K = 20$, rotation rate $\gamma = 0.1$, at azimuthal mode number $m = 20$.

Figure 4 to correspond to the lowest value of R_e at which the entire upper branch of eigenvalues first becomes unstable. It may be the case that this upper line of eigenvalues is, in fact, a continuum although this so far remains uncertain. In any event, the solution at $R_e = 30\,000$ in Figure 6(c) contains a very large number of eigenvalues with positive imaginary parts and real parts that are noninteger multiples. The (linearized) solution for this case therefore contains an unstable quasi-periodic orbit of very high dimension; this is the situation identified by Forbes [10, 11] as corresponding to true turbulence, particularly since the re-introduction of nonlinearity would cause this solution to collapse onto a strange attractor of very high dimension.

The final picture Figure 6(d) in this series is for the case $R_e = 50\,000$. As is evident from the diagram, the pattern of eigenvalues continues to move up into the unstable zone, with increasing Reynolds number. The upper line of eigenvalues is embedded in the region $\mathrm{Im}\{\Omega\} > 0$ and additional groups of them have also moved into this region of the complex Ω-plane. This movement evidently continues as R_e is increased, until eventually the pattern of eigenvalues is dominated by a structure similar to that in Figure 3, in which the eigenvalues are symmetrically located about the real axis, as described in Theorem 5.1.

The eigenvalues for the infinite Reynolds number solution for the case $K = m = 20$ are shown in Figure 7. Obtaining accurate results for very large Reynolds numbers is more difficult numerically for such large mode numbers K, m, and it is evident that the eigenvalues even with $N = 201$ modes have not quite converged in some regions of the complex Ω-plane. However, the convergence is excellent near the two corner regions

https://doi.org/10.1017/S1446181117000256 Published online by Cambridge University Press

at about $\mathrm{Re}\{\Omega\} = 21$, where the results for $N = 201$ and $N = 401$ are the same, at least to three significant figures. The distribution of eigenvalues is symmetric about the real axis, as proven in Theorem 5.1, which shows the destabilizing effect of the nonlinear viscosity terms, as in Figure 3.

The eigenfunctions $\widetilde{U}_1(r)$, $\widetilde{V}_1(r)$ and $\widetilde{W}_1(r)$ in equations (3.2) vary greatly in shape, depending on their corresponding eigenvalue Ω. A sample is shown in Figure 8, for the case $R_e = 50\,000$ plotted in Figure 6(d). This eigenmode in Figure 8 has been computed for the particular eigenvalue $\Omega = 8.8211 + 2.4042i$, chosen somewhat arbitrarily. This represents an unstable mode that grows exponentially in time (at least in the linearized theory studied here) and in these diagrams, the real part of the eigenfunction shown is plotted on the horizontal axis and the radius r is plotted vertically. For $\widetilde{U}_1(r)$ and $\widetilde{W}_1(r)$, the function and its first derivative are required to vanish at $r = 0$ and $r = 1$ (in dimensionless coordinates) according to equations (4.4), and $\widetilde{V}_1(r)$ must also vanish at these boundaries. This behaviour is evident in Figure 8. It is interesting that the function $\widetilde{U}_1(r)$ in Figure 8(a) is mostly focussed in a narrow cylinder near the centre $r = 0$ of the pipe, whereas the dominant region of the function $\widetilde{V}_1(r)$ in Figure 8(b) occurs near about $r = 0.8$. The axial component $\widetilde{W}_1(r)$ in Figure 8(c) is a combination of these previous two, as expected from the linearized continuity equation (3.3).

As indicated previously, the rotation speed γ does not greatly affect the nature of the solutions, although when very large it can have a stabilizing effect, as expected. This is illustrated in Figure 9. Here, the parameters have the same values $K = m = 20$ and $F = 600$ as in Figure 6, and eigenvalues distributions are shown for the same two Reynolds numbers $R_e = 30\,000$ and $R_e = 50\,000$ illustrated in Figures 6(c) and (d). In Figure 9, however, the rotation speed has been increased very greatly to $\gamma = 20$. The stabilizing effect is evident in Figure 9, since the pattern of eigenvalues has been pulled down towards the bottom of the diagram in both cases. For the flow at Reynolds number $R_e = 30\,000$, there are only a few discrete eigenvalues in the unstable zone $\mathrm{Im}\{\Omega\} > 0$ rather than the very large number of them that occurred with $\gamma = 0.1$ in Figure 6(c). Similarly, for the case $R_e = 50\,000$ the distribution of eigenvalues has been moved down towards the stable zone, although there is still the line of eigenvalues in the unstable zone $\mathrm{Im}\{\Omega\} > 0$, and these would again produce a high-dimensional quasi-periodic orbit, and therefore genuinely turbulent flow would be expected when nonlinear effects were taken into account.

To conclude this presentation of results, an eigenfunction is shown in Figure 10 for Reynolds number $R_e = 50\,000$ at the large rotation speed $\gamma = 20$, as in Figure 9, with all the other parameters unchanged. The particular eigenfunction shown here is for a stable mode with eigenvalue $\Omega = 416.18 - 7.8276i$, and has been chosen to illustrate an interesting mode in which the disturbance is zero over most of the pipe, and apparently only has compact support over the approximate interval $0.3 < r < 0.55$. This represents a cylindrical ring of fluid disturbance to the underlying Poiseuille–Couette flow in the pipe, with no perturbation near the centre $r = 0$ or the wall $r = 1$ (in dimensionless coordinates).

https://doi.org/10.1017/S1446181117000256 Published online by Cambridge University Press

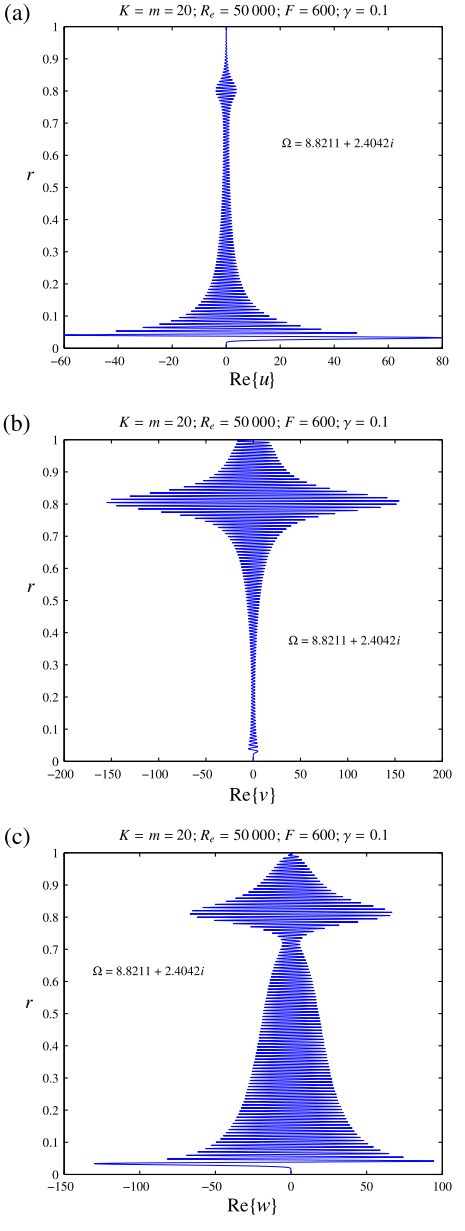

FIGURE 8. An unstable eigenfunction for the case $K = m = 20$, $F = 600$, $\gamma = 0.1$ and Reynolds number $R_e = 50\,000$, as illustrated in Figure 6(d). The particular eigenmode shown is for the eigenvalue $\Omega = 8.8211 + 2.4042i$. The real parts of the expressions for the three velocity components are displayed in (a) u, (b) v and (c) w.

https://doi.org/10.1017/S1446181117000256 Published online by Cambridge University Press

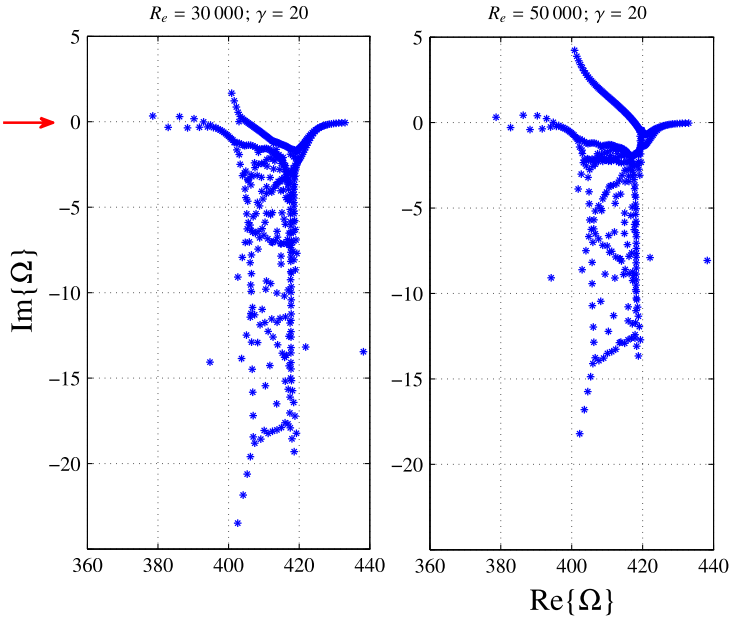

FIGURE 9. Eigenvalue distribution in the complex Ω-plane, for the two Reynolds numbers $R_e = 30\,000$ and $R_e = 50\,000$, with $K = m = 20$, $F = 600$ as in Figure 6, except that the rotation rate is $\gamma = 20$. The (red online) arrow at the left of the diagrams shows the stability boundary $\mathrm{Im}\{\Omega\} = 0$.

6. Conclusions

This paper has continued an investigation begun recently by Forbes [10] into the details of simple flow of a Reiner–Rivlin fluid, and its stability. In particular, it has been found that the pipe flow may become unstable at certain critical Reynolds numbers, which depend upon the second nonlinear viscosity coefficient τ (or $1/F$ in dimensionless variables). The instability may take one of two different structural forms, mathematically; the first is the classical type in which a single mode develops a positive growth rate, but the second involves a very large number – perhaps even a continuum – of eigenvalues moving into the unstable zone, over a small range of Reynolds numbers near some critical value. This second type produces an unstable solution that contains a very high-dimensional quasi-periodic solution, which in nonlinear theory is expected to produce a chaotic strange attractor of very high dimension, through the mechanism of Ruelle–Takens–Newhouse bifurcation (Thompson and Stewart, [32, p. 196]). It is suggested here, as in Forbes [10, 11] that this is an important contributor to the transition from laminar to turbulent flow, since under the high local rates of strain associated with turbulence, the linear Newtonian hypothesis underlying Navier–Stokes theory may no longer be entirely correct. This is consistent with the experimental findings of Pelton et al. [21]. As a result, some small degree of non-Newtonian behaviour would occur, the simplest example of which is

https://doi.org/10.1017/S1446181117000256 Published online by Cambridge University Press

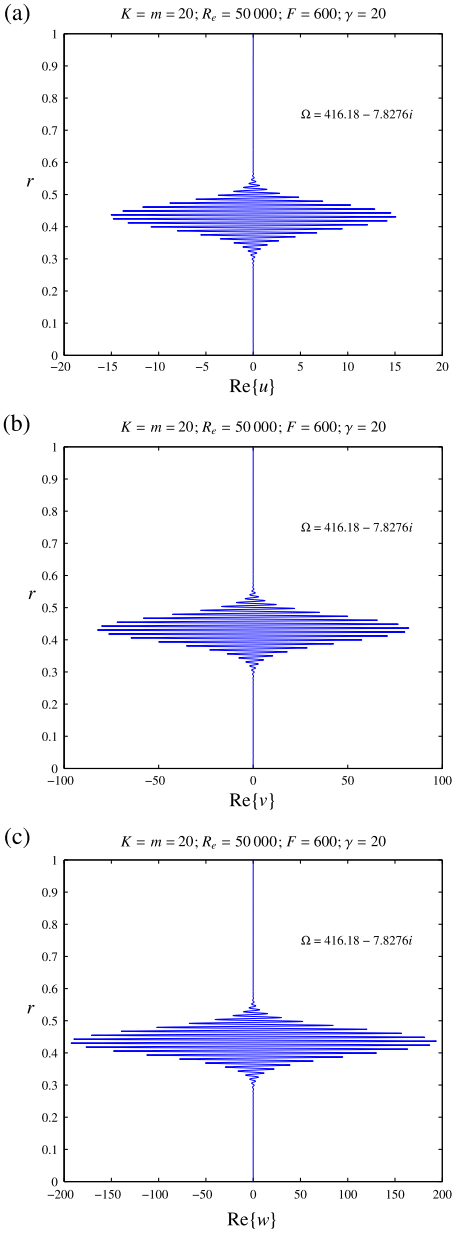

FIGURE 10. A stable eigenfunction for the case $K = m = 20$, $R_e = 50\,000$, $F = 600$ and rotation rate $\gamma = 20$, as illustrated in Figure 9. The particular eigenmode shown is for the eigenvalue $\Omega = 416.18 - 7.8276i$. The real parts of the expressions for the three velocity components are displayed in (a) u, (b) v and (c) w.

modelled in the Reiner–Rivlin equations. Since this has a destabilizing effect on the flow, it may be an important mechanism for triggering the onset of turbulence.

https://doi.org/10.1017/S1446181117000256 Published online by Cambridge University Press

Carrying out a classical linearized stability anaysis of a Reiner–Rivlin fluid is algebraically extremely complicated in non-Cartesian geometry, and particularly when coordinate singularities occur, such as at the centre line $r = 0$ of pipe flow in polar coordinates, as discussed here. This has been managed here using spectral solution forms, involving Bessel functions of the first kind. It has been found here that this can easily give systems of equations that are so extremely ill-conditioned that they are essentially unusable, and this was eventually overcome in the present paper using the bi-streamfunction approach of Section 2.5 to prompt the appropriate representation and spectral decomposition. Nevertheless, this results in algebraic systems that are so complicated as to be overwhelming for a person attempting to manipulate them, and errors can easily occur. We checked these systems by making extensive use of a computer symbolic-manipulation language, but even this was difficult and error-prone. However, as computers continue to become more sophisticated, it is easy to imagine that the process of setting up and solving such difficult systems will become more straightforward as software continues to develop. To overcome this problem here, however, a new matrix-based approach to the equations was developed, and has proven to be very successful.

The Reiner–Rivlin equations do possess linearized stability properties that agree at least qualitatively with experimental observation. For a fixed value of the nonlinear viscosity coefficient τ ($1/F$ in dimensionless variables) pipe flow is stable for low values of the Reynolds number R_e. But there is a critical Reynolds number at which a very large number of eigenvalues cross over into the unstable region in the complex plane, creating a quasi-periodic orbit of very high dimension; this would be expected to collapse onto a very high-dimensional chaotic attractor once nonlinear effects were taken into account. From a practical point of view, this would mean that, as Reynolds number was increased, the flow could be observed to make a transition from laminar to turbulent behaviour over a moderately narrow band of Reynolds numbers. This may account for experimental observations of transitional flows and seems worthy of further study.

The material nonlinearity terms with coefficient τ in the Reiner–Rivlin equation (2.3) have the effect of destabilizing the flow, and in some sense "compete" with the usual viscous terms with dynamic viscosity coefficient μ in equation (2.3), which act to stabilize the system. When material nonlinearity (non-Newtonian behaviour) dominates, we proved in Theorem 5.1 that eigenvalues occur in complex conjugate pairs, meaning that such flows must be unstable; the inclusion of nonlinear effects would then be expected to generate "elasto-inertial turbulence" as described by Samanta et al. [27]. (It is interesting to note that the transformations (5.1) were first observed in the numerical results and only later verified analytically as here). As suggested by Forbes [10], it may therefore be the case that there is a connection between the regular type of turbulent behaviour commonly encountered in water or air and the more exotic low-speed turbulence seen in polymer fluids (for example, see Larson [16]), since both could possibly lie on the same or similar mathematical solution branch.

https://doi.org/10.1017/S1446181117000256 Published online by Cambridge University Press

The results discussed here clearly present a great many further questions, which are outside the scope of this present investigation, but seem worthy of future study. We have begun initial work on whether the linearized Reiner–Rivlin equations are capable of supporting an approximate form of the coherent structures found by Waleffe [36]; numerical work seems to confirm this, but much remains still to be done. The inclusion of nonlinearity in flows such as that studied here is also of interest, and the possible connection with elasto-inertial turbulence in highly non-Newtonian materials is a rich avenue for further research.

Appendix A. Momentum equations

This appendix presents the full linearized momentum equations used in the text.

The azimuthal θ-momentum equation after linearization is given by equation (3.5), in which the majority of the terms in the equation are encapsulated in the function

$$\begin{aligned}\mathbf{T}(r) = {} & -2v_0'\widetilde{U}_1 - imv_0'\widetilde{V}_1 - ikw_0(r)\widetilde{V}_1 \\ & + \frac{\mu}{\rho}\Big[\sum_{n=1}^{N} B_n T_n^{4b} + k^2\sum_{n=1}^{N} B_n T_n^{2b} + \frac{2mk}{r^2}\sum_{n=1}^{N} A_n T_n^{1a}\Big] \\ & + \frac{2\tau}{\rho}w_0''\Big[\frac{1}{2}\Big(ik\widetilde{V}_1 + \frac{im}{r}\widetilde{W}_1\Big) + \frac{1}{4}\Big(2ikr\widetilde{V}_1' - mk\widetilde{U}_1 + im\widetilde{W}_1'\Big)\Big].\end{aligned} \tag{A.1}$$

The linearized r-momentum equation (3.6) for the radial coordinate similarly involves the complicated function

$$\begin{aligned}\mathbf{R}(r) = {} & -imv_0'\widetilde{U}_1 + 2v_0'\widetilde{V}_1 - ikw_0(r)\widetilde{U}_1 + \frac{\mu}{\rho}\Big[-\frac{im}{r}\sum_{n=1}^{N} B_n T_n^{3b} - \frac{im}{r}k^2\sum_{n=1}^{N} B_n T_n^{1b} \\ & + ik\sum_{n=1}^{N} A_n T_n^{3a} + ik\Big(k^2 - \frac{2m}{r^2}\Big)\sum_{n=1}^{N} A_n T_n^{1a}\Big] \\ & + \frac{2\tau}{\rho}w_0''\Big[\widetilde{W}_1' + ik\widetilde{U}_1 - \frac{1}{4}\Big(mk\widetilde{V}_1 + \frac{m^2}{r}\widetilde{W}_1\Big) + \frac{1}{2}r\Big(\widetilde{W}_1'' + 2ik\widetilde{U}_1' - k^2\widetilde{W}_1\Big)\Big].\end{aligned} \tag{A.2}$$

The final function involved in the axial z-momentum equation (3.7) is given by the formula

$$\begin{aligned}\mathbf{Z}(r) = {} & -w_0''r\widetilde{U}_1 - imv_0'\widetilde{W}_1 - ikw_0(r)\widetilde{W}_1 - \frac{\mu}{\rho}\Big[\frac{2m}{r^2}\sum_{n=1}^{N} A_n T_n^{5a} + \frac{1}{r}\sum_{n=1}^{N} A_n T_n^{3a} \\ & + \frac{k^2}{r}\sum_{n=1}^{N} A_n T_n^{1a} + \sum_{n=1}^{N} A_n T_n^{4a} + k^2\sum_{n=1}^{N} A_n T_n^{2a}\Big] + \frac{2\tau}{\rho}w_0''\Big[\widetilde{U}_1' + ik\widetilde{W}_1 \\ & + \frac{1}{4}\Big(im\widetilde{V}_1' - \frac{im}{r}\widetilde{V}_1 - \frac{m^2}{r}\widetilde{U}_1\Big) + \frac{1}{2}r\Big(\widetilde{U}_1'' + 2ik\widetilde{W}_1' - k^2\widetilde{U}_1\Big)\Big].\end{aligned} \tag{A.3}$$

https://doi.org/10.1017/S1446181117000256 Published online by Cambridge University Press

The constant μ is the Newtonian coefficient of dynamic viscosity and τ is the second viscosity coefficient in the non-Newtonian term, as in equation (2.3). The background axial velocity component $w_0(r)$ is given by (2.11) and $v_0(r)$ is the azimuthal velocity component (2.13).

In the expressions (A.1)–(A.3), the four functions T_n^{1b}, T_n^{1a}, T_n^{2b} and T_n^{2a} are already given in equation (4.5) and the remaining such intermediate functions are

$$\begin{aligned}
T_n^{3b}(r) &= \beta_{mn}[\beta_{mn}J_m(\beta_{mn}r) - \beta_{m,N+1}\mathcal{M}_{mn}J_m(\beta_{m,N+1}r)],\\
T_n^{3a}(r) &= \alpha_{mn}[\alpha_{mn}J_{m+1}(\alpha_{mn}r) - \alpha_{m,N+1}\mathcal{N}_{mn}J_{m+1}(\alpha_{m,N+1}r)],\\
T_n^{4b}(r) &= \beta_{mn}[\beta_{mn}^2J'_m(\beta_{mn}r) - \beta_{m,N+1}^2\mathcal{M}_{mn}J'_m(\beta_{m,N+1}r)],\\
T_n^{4a}(r) &= \alpha_{mn}[\alpha_{mn}^2J'_{m+1}(\alpha_{mn}r) - \alpha_{m,N+1}^2\mathcal{N}_{mn}J'_{m+1}(\alpha_{m,N+1}r)],\\
T_n^{5a}(r) &= \alpha_{mn}[J_{m+2}(\alpha_{mn}r) - \mathcal{N}_{mn}J_{m+2}(\alpha_{m,N+1}r)].
\end{aligned} \tag{A.4}$$

In the last expression in the system (A.4), a recurrence relation was used to obtain the Bessel function J_{m+2}, following Abramowitz and Stegun [1, p. 361]. The constants $\mathcal{M}_{mn}$ and $\mathcal{N}_{mn}$ are as defined in equation (4.3) in the text. The first term on the right-hand side of (A.3) is a consequence of the identity $w_0'(r) = w_0''r$, which follows at once from Poiseuille flow (2.11).

Acknowledgements

This work is associated with Australian Research Council Discovery Grant DP140100094. We are grateful for comments from two anonymous referees.

References

[1] M. Abramowitz and I. A. Stegun, *Handbook of mathematical functions* (Dover, New York, NY, 1972).
[2] R. Aris, *Vectors, tensors and the basic equations of fluid mechanics* (Dover, New York, NY, 1962).
[3] G. K. Batchelor, *An introduction to fluid dynamics* (Cambridge University Press, Cambridge, 1967).
[4] C. Cambon and J. F. Scott, "Linear and nonlinear models of anisotropic turbulence", *Annu. Rev. Fluid Mech.* **31** (1999) 1–53; doi:10.1146/annurev.fluid.31.1.1.
[5] S. Cherubini, P. De Palma, J.-Ch. Robinet and A. Bottaro, "A purely nonlinear route to transition approaching the edge of chaos in a boundary layer", *Fluid Dyn. Res.* **44** (2012) 031404, 11 pages; doi:10.1088/0169-5983/44/3/031404.
[6] P. A. Davidson, *Turbulence: An introduction for scientists and engineers* (Oxford University Press, Oxford, 2004).
[7] P. G. Drazin and W. H. Reid, *Hydrodynamic stability*, 2nd edn (Cambridge University Press, Cambridge, 2004).
[8] B. Eckhardt, "Turbulence transition in pipe flow: some open questions", *Nonlinearity* **21** (2008) T1–T11; doi:10.1088/0951-7715/21/1/T01.
[9] B. Eckhardt, "Turbulence transition in shear flows: chaos in high-dimensional spaces", *Procedia IUTAM* **5** (2012) 165–168; doi:10.1016/j.piutam.2012.06.021.
[10] L. K. Forbes, "On turbulence modelling and the transition from laminar to turbulent flow", *ANZIAM J.* **56** (2014) 28–47; doi:10.1017/S1446181114000224.

[11] L. K. Forbes, "Transition to turbulence from plane Couette flow", *ANZIAM J.* **57** (2015) 89–113; doi:10.1017/S1446181115000176.
[12] W. K. George, *Lectures in turbulence for the 21st century* (Turbulence Research Lab., Chalmers University, Gothenburg, Sweden, 2013); http://www.turbulence-online.com.
[13] T. L. Harman, J. Dabney and N. Richert, *Advanced engineering mathematics with MATLAB*, 2nd edn (Brooks & Cole, Pacific Grove, CA, 2000).
[14] P. A. Kelly, *Foundations of continuum mechanics* (The University of Auckland, Auckland, New Zealand, 2015); http://homepages.engineering.auckland.ac.nz/~pkel015/SolidMechanicsBooks/Part_III/index.html (Last updated: 24 February 2015).
[15] V. Kitsios, L. Cordier, J.-P. Bonnet, A. Ooi and J. Soria, "Development of a nonlinear eddy-viscosity closure for the triple-decomposition stability analysis of a turbulent channel", *J. Fluid Mech.* **664** (2010) 74–107; doi:10.1017/S0022112010003617.
[16] R. G. Larson, "Fluid dynamics—turbulence without inertia", *Nature* **405** (2000) 27–28; doi:10.1038/35011172.
[17] W. D. McComb, "Theory of turbulence", *Rep. Progr. Phys.* **58** (1995) 1117–1206; doi:10.1088/0034-4885/58/10/001.
[18] A. N. Morozov and W. van Saarloos, "Subcritical finite-amplitude solutions for plane Couette flow of viscoelastic fluids", *Phys. Rev. Lett.* **95** (2005) 024501, 4 pages; doi:10.1103/PhysRevLett.95.024501.
[19] S. A. Orszag, "Accurate solution of the Orr–Sommerfeld stability equation", *J. Fluid Mech.* **50** (1971) 689–703; doi:10.1017/S0022112071002842.
[20] L. Pan, A. Morozov, C. Wagner and P. E. Arratia, "Nonlinear elastic instability in channel flows at low Reynolds numbers", *Phys. Rev. Lett.* **110** (2013) 174502, 5 pages; doi:10.1103/PhysRevLett.110.174502.
[21] M. Pelton, D. Chakraborty, E. Malachosky, P. Guyot-Sionnest and J. E. Sader, "Viscoelastic flows in simple liquids generated by vibrating nanostructures", *Phys. Rev. Lett.* **111** (2013) 244502, 5 pages; doi:10.1103/PhysRevLett.111.244502.
[22] R. J. Poole, "The Deborah and Weissenberg numbers. The British Society of Rheology", *Rheology Bulletin* **53** (2012) 32–39; http://pcwww.liv.ac.uk/~robpoole/PAPERS/POOLE_45.pdf.
[23] M. Reiner, "A mathematical theory of dilatancy", *Amer. J. Math.* **67** (1945) 350–362; http://www.jstor.org/stable/2371950.
[24] O. Reynolds, "On the dynamical theory of incompressible viscous fluids and the determination of the criterion", *Philos. Trans. R. Soc. Lond. A* **186** (1895) 123–164; http://www.jstor.org/stable/90643.
[25] R. S. Rivlin, "The hydrodynamics of non-Newtonian fluids. I", *Proc. R. Soc. Lond. A* **193** (1948) 260–281; http://www.jstor.org/stable/97992.
[26] R. S. Rivlin., "The relation between the flow of non-Newtonian fluids and turbulent Newtonian fluids", *Quart. Appl. Math.* **15** (1957) 212–215; http://www.jstor.org/stable/43634450.
[27] D. Samanta, Y. Dubief, M. Holzner, C. Schäfer, A. N. Morozov, C. Wagner and B. Hof, "Elasto-inertial turbulence", *Proc. Natl. Acad. Sci. USA* **110** (2013) 10557–10562; doi:10.1073/pnas.1219666110.
[28] M. Sano and K. Tamai, "A universal transition to turbulence in channel flow", *Nat. Phys.* **12** (2016) 249–253; doi:10.1038/nphys3659.
[29] E. S. G. Shaqfeh, "Purely elastic instabilities in viscometric flows", *Annu. Rev. Fluid Mech.* **28** (1996) 129–185; doi:10.1146/annurev.fl.28.010196.001021.
[30] C. G. Speziale, "On nonlinear $K-\ell$ and $K-\varepsilon$ models of turbulence", *J. Fluid Mech.* **178** (1987) 459–475; doi:10.1017/S0022112087001319.
[31] H. B. Squire, "On the stability for three-dimensional disturbances of viscous fluid flow between parallel walls", *Proc. R. Soc. Lond. A* **142** (1933) 621–628; doi:10.1098/rspa.1933.0193.
[32] J. M. T. Thompson and H. B. Stewart, *Nonlinear dynamics and chaos* (Wiley, New York, 1986).
[33] L. N. Trefethen, A. E. Trefethen, S. C. Reddy and T. A. Driscoll, "Hydrodynamic stability without eigenvalues", *Science* **261** (1993) 578–584; doi:10.1126/science.261.5121.578.

[34] J. V. Valério, M. S. Carvalho and C. Tomei, "Efficient computation of the spectrum of viscoelastic flows", *J. Comput. Phys.* **228** (2009) 1172–1187; doi:10.1016/j.jcp.2008.10.018.
[35] G. von Winckel, lgwt.m. Written 2004. at: MATLAB file exchange website; http://au.mathworks.com/matlabcentral/fileexchange/4540-legendre-gauss-quadrature-weights-and-nodes.
[36] F. Waleffe, "Exact coherent structures in channel flow", *J. Fluid Mech.* **435** (2001) 93–102; doi:10.1017/S0022112001004189.